

# Deep inside the core of Abell 1795: the *Chandra* view

S. Ettori<sup>1,2</sup>, A.C. Fabian<sup>1</sup>, S.W. Allen<sup>1</sup> and R.M. Johnstone<sup>1</sup>

<sup>1</sup> Institute of Astronomy, Madingley Road, CB3 0HA Cambridge

<sup>2</sup> ESO, Karl-Schwarzschild-Str. 2, D-85748 Garching, Germany

Resubmitted 2001 November 23. Submitted 2001 May 9.

## ABSTRACT

We present X-ray spatial and spectral analysis of the *Chandra* data from the central 400  $h_{50}^{-1}$  kpc of the cluster of galaxies Abell 1795. The plasma temperature rises outwards by a factor of 3, whereas the iron abundance decreases by a factor of 4. The spatial distribution of Oxygen, Neon, Sulphur, Silicon and Iron shows that supernovae Type Ia dominate the metal enrichment process of the cluster plasma within the inner 150 kpc. Resolving both the gas density and temperature in 9 radial bins, we recover the gravitational mass density profile and show that it flattens within 100 kpc as  $\rho_{\text{DM}} \propto r^{-0.6}$  with a power law index flatter than  $-1$  at  $> 3\sigma$  level. The observed motion of the central galaxy and the presence of excesses and deficits along the North-South direction in the brightness distribution indicate that the central cluster region is not relaxed. In the absence of any non-gravitational heating source, the data from the inner  $\sim 200$  kpc indicate the presence of a cooling flow with an integrated mass deposition rate of about  $100 M_{\odot} \text{ yr}^{-1}$ . Over the same cluster region, the observed rate of  $74 M_{\odot} \text{ yr}^{-1}$  is consistent with the recent *XMM-Newton* Reflection Grating Spectrometer limit of  $150 M_{\odot} \text{ yr}^{-1}$ .

**Key words:** galaxies: clusters: individual: A1795 – dark matter – X-ray: galaxies.

## 1 INTRODUCTION

Abell 1795 (Abell, Corwin & Olowin 1989) is a nearby rich cD galaxy cluster well studied at optical, radio and X-ray wavelengths. In X-rays, it shows a relaxed structure (Buote & Tsai 1996) and a surface brightness strongly peaked in the centre, where cooler gas is present (Fabian 1994, Briel & Henry 1996, Allen & Fabian 1997, Ikebe et al. 1999, Allen et al. 2001, Tamura et al. 2001). Strong optical emission lines around the cD galaxy (Cowie et al. 1983), an excess in the blue optical light (Johnstone, Fabian & Nulsen 1987; Cardiel, Gorgas & Aragon-Salamanca 1997) and emission in ultraviolet (Mittaz et al. 2001) due to the formation of massive stars, perhaps triggered by the central radio source 4C 26.42 (McNamara et al. 1996), support a scenario in which the central peak of cooler gas is due to a massive cooling flow (Edge et al. 1992, Fabian 1994).

In a previous paper (Fabian et al. 2001b), we have presented a spatial analysis in three X-ray colors of the *Chandra* observation of the core of A1795. In the present work, we analyze the spectral characteristics of the intracluster medium, studying the metal enrichment, deprojecting the physical properties and determining the form of the gravitational potential within the cluster core.

Hereafter, we assume the values of the cosmological parameters to be  $H_0 = 50 \text{ km s}^{-1} \text{ Mpc}^{-1}$ ,  $\Omega_m = 1$ ,  $\Omega_{\Lambda} = 0$ . At the nominal redshift of A1795 ( $z = 0.0632$ , Girardi et al. 1998), an angular scale of 1 arcsec ( $\sim 2$  ACIS pixels) corresponds to a physical length of 1.65 kpc. For the currently popular cosmology of  $(H_0, \Omega_m, \Omega_{\Lambda}) = (70, 0.3, 0.7)$ , distances change by a factor of 0.74, luminosity by  $0.74^2 = 0.54$  and the age of the Universe at the cluster redshift by 1.06.

All the errors quoted are  $1\sigma$  (68.3 per cent level of confidence) unless stated otherwise.

## 2 *Chandra* DATASETS

In Table 1, we present a summary of the *Chandra* (Weiskopf et al. 2000) observations which were both made with the back-illuminated CCD S3 of the Advanced Camera for Imaging and Spectroscopy (ACIS) instrument. We have used the CIAO software (version 2.1) to clean further the revision-1 level-2 events files provided by the standard pipeline processing that filters for ASCA grade classifications of 0,2,3,4,6 and defines Good Time Intervals for a nominal total exposure given in parenthesis in Table 1. The FP-120° dataset has been analyzed with the August 2001 release of of ACIS response products (Fits Encoded Function and gain files; see at [http://asc.harvard.edu/cal/Links/Acis/acis/Cal\\_prods/matrix/matrix.html](http://asc.harvard.edu/cal/Links/Acis/acis/Cal_prods/matrix/matrix.html)), whereas the FP-110° events file is calibrated according to the previous release of December 1999. Therefore the original FP-120° dataset has been reprocessed with *acis\_process\_events* routine in CIAO 2.1.3 with the gain files available in CALDB 2.7. We have also corrected for time intervals with (i) bad attitude solutions, and (ii) high background with flares in the lightcurve with relative value larger than 20 per cent the mean count rate. This process reduces the effective exposure by about 5 per cent in the two datasets.

**Table 1.** *Chandra* observations summary of A1795. “BI” stands for “Back Illuminated CCD”. The temperature to which the Focal Plane (FP) is cooled is given for each exposure. As discussed in the text, this temperature is relevant for the definition of the calibration files.

Chip	Date	Exposure (sec)
BI-S3, FP-110°	20 Dec 1999	18370 (19522)
BI-S3, FP-120°	21 Mar 2000	18927 (19627)

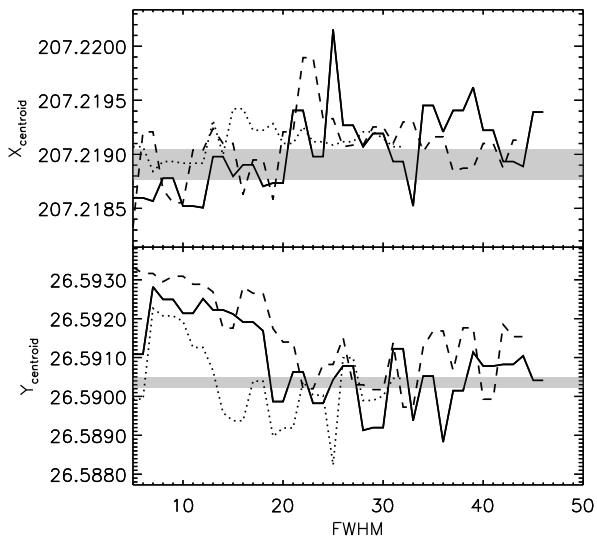


**Figure 1.** X-ray centre (shaded region with a width of 1 arcsec) and centroids estimated within a box with half-width equal to  $0.637 \times \text{FWHM}$  in units of arcsec (routine CNTRD in Interactive Data Language) and in three different X-ray colour images (0.5 – 0.8 keV band: solid line; 0.8 – 1.5 keV band: dotted line; 1.5 – 7 keV band: dashed line).

### 3 IMAGING ANALYSIS

The optical position of the cD (which hosts the radio source 4C+26.42) is (RA, Dec)  $13^{\text{h}} 48^{\text{m}} 52^{\text{s}}.43$ ,  $26^{\circ} 35' 34''.0$  (J2000). This is within the  $5 \times 5$  arcsec<sup>2</sup> bright envelope to the north of the X-ray emitting wake, also known as an H $\alpha$  emitter, discussed in our previous work (Fabian et al. 2001b). The X-ray centre for our analysis is chosen at coordinates (RA, Dec)  $13^{\text{h}} 48^{\text{m}} 52^{\text{s}}.54$ ,  $26^{\circ} 35' 25''.3$  (J2000). This is consistent with the centroid of the X-ray emission determined in three different X-ray colour images. The behaviour of the centroid and the chosen centre are plotted in Fig. 1.

The choice of the centre is also determined to make circular annuli a good representation of the cluster surface brightness as shown in Fig. 2. This is relevant in the deprojection analysis applied in the present work that assumes a spherical symmetric emission projected on the sky in circular regions.

The azimuthally averaged brightness profile is shown in Fig. 3. Two main breaks are evident at about 25 and 300 kpc, respectively, when the profile is compared with a smoothed distribution provided, e.g., from a  $\beta$ -model (e.g. Cavaliere & Fusco-Femiano 1976) fitted over the radial range 0–400 kpc (with best-fit parameters  $r_c = 49 \pm 1$  kpc,  $\beta = 0.510 \pm 0.002$ ,  $\chi^2 = 971$ , 243 degrees of freedom). The presence of breaks in the brightness distribution is now routinely observed in *Chandra* data of galaxy clusters (e.g. Allen, Ettori, Fabian 2001, Markevitch et al. 2001, Vikhlinin et al.

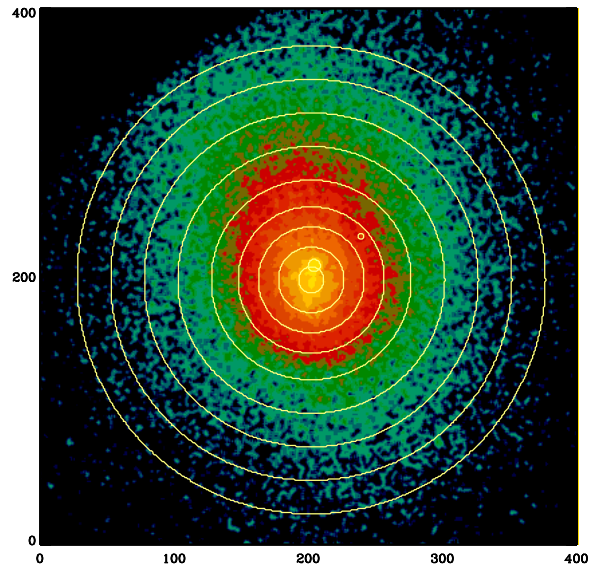


**Figure 2.** Annuli adopted in the spectral analysis overlaid to a smoothed image of A1795 (units in pixel = 0.984 arcsec).

2001, Mazzotta et al. 2001) and is mainly associated with discontinuities in the gas density profile probably due either to the aggregation of subclumps or to the “sloshing” of the gas decoupled from dark matter into the changing gravitational potential (as suggested for the break in the surface brightness about  $70''$  southward the central galaxy in A1795 from Markevitch, Vikhlinin & Mazzotta 2001).

It is worth noting that a  $\beta$ -model is generally not a good representation of the brightness profile of cooling flow clusters, like A1795, over large radial ranges due to the peaked central emission (but see improvements in modelling this kind of profiles obtained from *Rosat* PSPC observations in Mohr et al. 1999 and Ettori 2000). When the central 200 kpc radius region is not included in the fit, Ettori & Fabian (1999) measure from a *Rosat* PSPC observation that extends up to 1.5 Mpc a core radius of 250 kpc and a  $\beta$  of 0.75, consistent with results from fits that include a model for the central excess (Mohr et al. 1999, Ettori 2000). Due to the strong positive correlation between core radius and  $\beta$  parameter, the evidence of a smaller core in the brightness profile as observed from *Chandra* implies a lower value of  $\beta$  as estimated. Moreover, it is interesting to note the dependence of these parameters from the radial range considered. For example, we find that, from a statistical point of view, the best modelling with a  $\beta$ -model in the central 400 kpc of A1795 is obtained over the range 0–60 kpc ( $\chi^2/\text{dof} = 45/34$ , probability  $P=0.09$ ), with best-fit parameters  $r_c = 23 \pm 2$  kpc and  $\beta = 0.353 \pm 0.011$  that show a significant lower value of  $r_c$  and a corresponding lower value of  $\beta$ . We remind, however, that the  $\beta$ -model is a convenient fitting function that assumes both an isothermal gas and the hydrostatic equilibrium between the galaxy population, the intracluster plasma and the underlying gravitational potential. In the cooling flow regions, the assumption of isothermality is definitely not correct and also the hydrostatic condition might be violated.

In Fig. 3, we show a map of the differences,  $(I - M)/\sqrt{M}$ , between the unsmoothed exposure corrected image,  $I$ , and the two-dimensional distribution of a smoothed model,  $M$ , that we choose

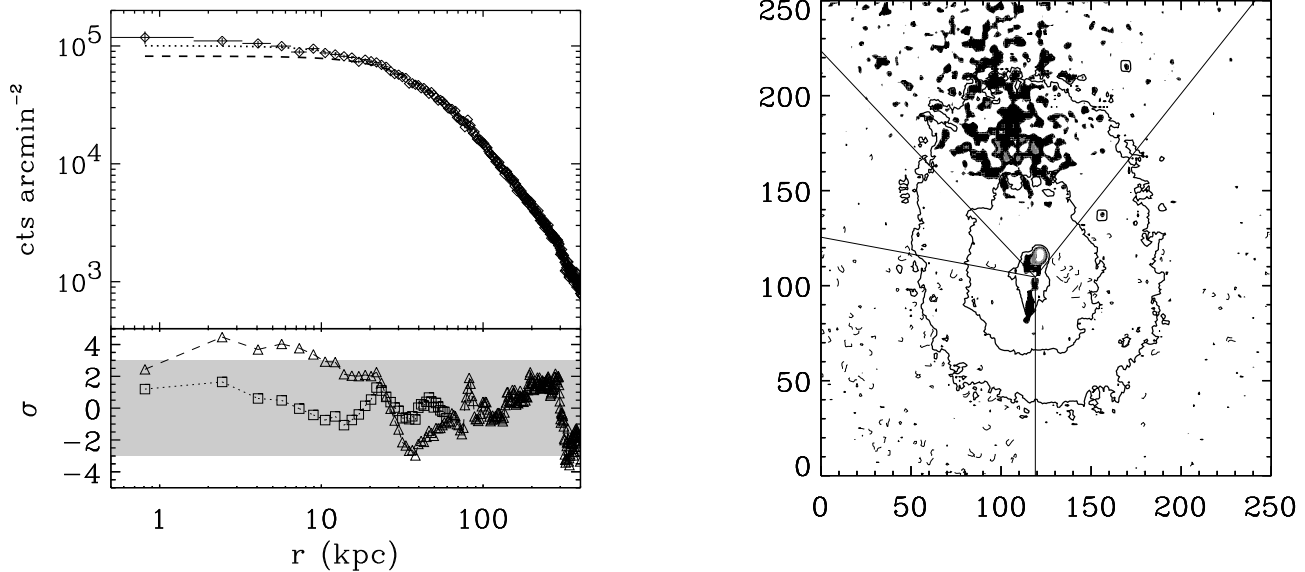


**Figure 3.** (Left) The azimuthally averaged brightness profile after background subtraction and exposure correction is shown. Overplotted are two  $\beta$ -model, one fitted on 0–60 kpc (dotted line and squares), the other over the 0–400 kpc radial range (dashed line and triangles). The differences in  $\sigma$  with respect to the model are smoothed over 5 bins for sake of clarity. Two main breaks are evident, at about 25 and 300 kpc, respectively. The shaded region indicates deviations within  $\pm 3\sigma$ . (Right)  $250 \times 250$  ( $1''$ -bin) $^2$  ( $\sim 410 \times 410$  kpc $^2$ ) map, smoothed on a 3 arcsec scale, of the differences between the original exposure corrected image and the two-dimensional distribution of a  $\beta$ -model fitted over the 0–400 kpc radial range (dashed line in the panel on the left). The shaded regions indicate positive values of  $(I - M)/\sqrt{M}$ , whereas dotted contours shows negative values. These deviations have an absolute value that ranges between 1 and 3. The lines that depart from the cross delimit the sectors in exam in Fig. 4.

to be a  $\beta$ -model with parameters constrained over the radial range 0–400 kpc. Note that positive excesses are present corresponding to (i) the central 20 arcsec-radius structure (i.e. cD galaxy plus filament) and (ii) extended emission 50 arcsec from the centre towards North-East. Negative values are predominant in the South-East direction.

The evidence for regions with an excess/deficit in emission along the North-South direction, but not aligned, becomes clear when the brightness profiles extracted in these sectors are compared to the emission from westward of the centre (Fig. 4). Starting at about 50 kpc, the excess in the North-East and the deficit in the South-East become evident with deviations respective to the West region of about  $10\sigma$ . This suggests that the core is in a non-relaxed status with indication of merging activity. In Sect. 5.4, we discuss more on the dynamical status of the cluster core.

### 3.1 X-ray colour profile

To study the spatial distribution of the photons with respect to their energy, we extract images in two X-ray ‘colours’ (0.5–1.5 keV, 1.5–7 keV), correct them by the respective exposure maps and subtract the background estimated from blank fields (see further comments in Sect. 5.2). The surface brightness profiles are then obtained in bins of 20 physical pixels (equal to 9.8 arcsec) and the color ratios determined (see Fig. 5)

The colour ratio rapidly decreases and flattens moving outwards, indicating a hardening in the photon counts. We have quantified this in a non-parametric way, calculating a weighted average (and relative error) of the colour ratio for all the points above a given radius. Then, a distribution of the number of points enclosed within a given colour ratio  $\pm 3\sigma$  is obtained. The values correspond-

ing to (16, 50, 84) per cent of the cumulative function of this distribution is plotted in Fig. 5. The break between the “most-probable” value and the rapid increase of the profile in the centre is located at  $r = 72^{+40}_{-32}$  arcsec ( $119^{+66}_{-53}$  kpc).

This excess of the relative amount of soft ( $< 1.5$  keV) photons with respect to the harder counts population traces the region with a lower gas temperature. Whether this gas is cooling or just following the behaviour of the gravitational potential is discussed in the following sections.

## 4 SPECTRAL ANALYSIS

The spectra were extracted from the processed events-2 files, selecting in PI space for energies between 0.5 and 7 keV to minimize the effects both of the uncertainties in the calibration of the observed soft X-rays and of the cosmic rays that dominate the background components at energies larger than 5 keV (see at the page <http://asc.harvard.edu/cal/Links/Acis/acis/Calprods/bkgrnd/current/index.html> maintained by M. Markevitch). The background spectrum has been extracted from the same region of the CCD in exam from blank field exposures (namely `aciss_B_s3_bg_evt_060600.fits` and `aciss_C_s3_bg_evt_191000.fits` for FP-110° and FP-120°, respectively) adapted to our observations through the routine `make_acisbg` provided to the *Chandra* community by M. Markevitch. As presented in Table 2, the total counts rate estimated in each ring in the adopted 0.5–7 keV energy range is contaminated from the background by a percentage between less than 1 per cent (in the inner annulus) and 4 per cent (in the outer ring), making this correction lower than statistical uncertainties.

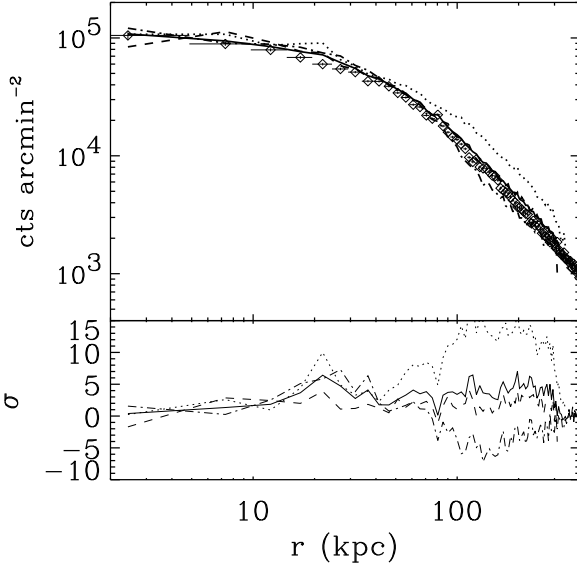


**Figure 4.** Brightness profiles extracted from four sectors ( $x$  axis at  $0^\circ$ ,  $y$  axis at  $90^\circ$ ; cf. Fig. 3):  $50^\circ$ – $135^\circ$  (“Northern excess”, dotted line),  $135^\circ$ – $170^\circ$  (dashed line),  $170^\circ$ – $270^\circ$  (“Southern deficit”, dot-dashed line),  $270^\circ$ – $50^\circ$  (diamonds). The azimuthally averaged profile is represented with a solid line. The residuals are plotted with respect to the “ $270^\circ$ – $50^\circ$ ” profile.

Redistribution Matrix Files (RMF) and Auxiliary Response Files (ARF) were made by averaging over a  $32 \times 32$  pixel-grid of calibration files covering the back-illuminated chip 7, using the CIAO tools *mkrmf* and *mkarf* and using weighting factors equal to the number of counts in the source in the region covered by the calibration.

In the present analysis, we use both single-phase and multi-phase models, considering that we are mapping the very central part of the cluster core. The single-phase model just assumes an emission from an optically-thin plasma (MEKAL –Kaastra 1992, Liedhal et al. 1995– in XSPEC v. 11.1.0 –Arnaud 1996) absorbed by a column density that we have left free to vary (hereafter, model *abs1T*; the reference column density is the Galactic value of  $1.2 \times 10^{20} \text{ cm}^{-2}$  from radio HI maps in Dickey & Lockman 1990).

The multi-phase model combines thermal emission from the ambient, outer gas with a continuous distribution of gas states represented by a cooling-flow model (Johnstone et al. 1992). An absorbing column density fixed to the Galactic value is put in front of the combined model. The cooling-flow component is also intrinsically absorbed by uniformly distributed amount of hydrogen atoms per  $\text{cm}^2$  at the cluster redshift that is left free to vary during the search for a minimum  $\chi^2$  (*absCF* model). The temperature and metallicity of the cooling-flow model are fixed to be equal to the ones of the thermal component. All the absorption of X-rays due to the interstellar medium has been parametrized using the Tübingen-Boulder model (TBABS in XSPEC v. 11.1.0; Wilms, Allen & McCray 2000).

Two representative spectra are shown in Figure 6 with the respective *abs1T* model. In Table 2, we quote the best-fit results for the gas temperature and metallicity obtained with a single-phase plasma model (*abs1T*) and with a multi-phase component (*absCF*). The minimum  $\chi^2$  and the number of degrees of freedom for these models are quoted in Table 3. In Figure 7, we plot the best-fit val-

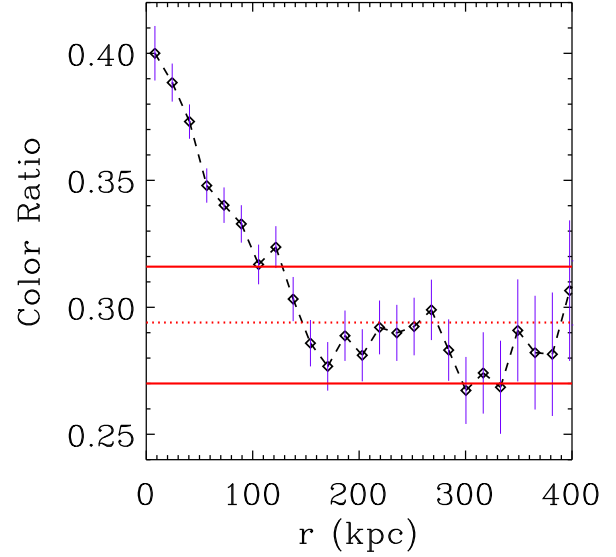


**Figure 5.** Color Ratio  $[(\text{soft-hard})/(\text{soft+hard})]$  obtained using the X-ray surface brightness profiles in the 0.5–1.5 keV and 1.5–7 keV band. Note how these colour ratios flatten at about 70 arcsec, equivalent to about 120 kpc.

ues obtained with the model *abs1T* for some interesting quantities and, where available, the region of uncertainty at the 90 per cent confidence level from the analysis of *ASCA* data in Allen (2000). Steep temperature and metallicity profiles are present within the inner 300 kpc. The emission-weighted gas temperature increases from 3.4 to 6.5 keV, whereas the metal abundance decreases with radius from about 0.7 times the solar photospheric values in Anders & Grevesse (1989) to  $\sim 0.2$ . The column density is consistent with the Galactic value above 50 kpc, but it is higher by a factor of 2 in the inner two annuli. A remarkable good agreement is present between the redshift measured independently in each ring and the optical estimate from Girardi et al. (1998).

In Fig. 8 and Table 3, we show that (i) the null-hypothesis probability on the goodness of the fits is larger than 0.1 on 6 out of nine annuli for both the *abs1T* and *absCF* models with the worst reduced  $\chi^2$  of about 1.27 in the second and sixth annulus, and (ii) that the cooling flow model, *absCF*, is equivalent to the single-phase model, *abs1T*, from a statistical point of view when the F (Fisher) test is considered (e.g. Bevington & Robinson 1992; on how a single-phase gas can mimic a multi-phase medium through projection effects see, e.g., Ettori 2001).

In the same Fig. 8, we compare also the spectral results for the FP-110° and FP-120° datasets. Gas temperatures, metallicities and column densities show differences generally between 1 and  $3\sigma$  and a clear trend with temperature and metal abundance estimates higher and column density values lower in the FP-120° dataset.

## 5 DEPROJECTION ANALYSIS OF THE SPECTRAL AND IMAGING DATA

In this Section, we discuss the constraints on the physical quantities obtained from the deprojection analysis applied to both the best-fit results of the spectral analysis presented in the previous section

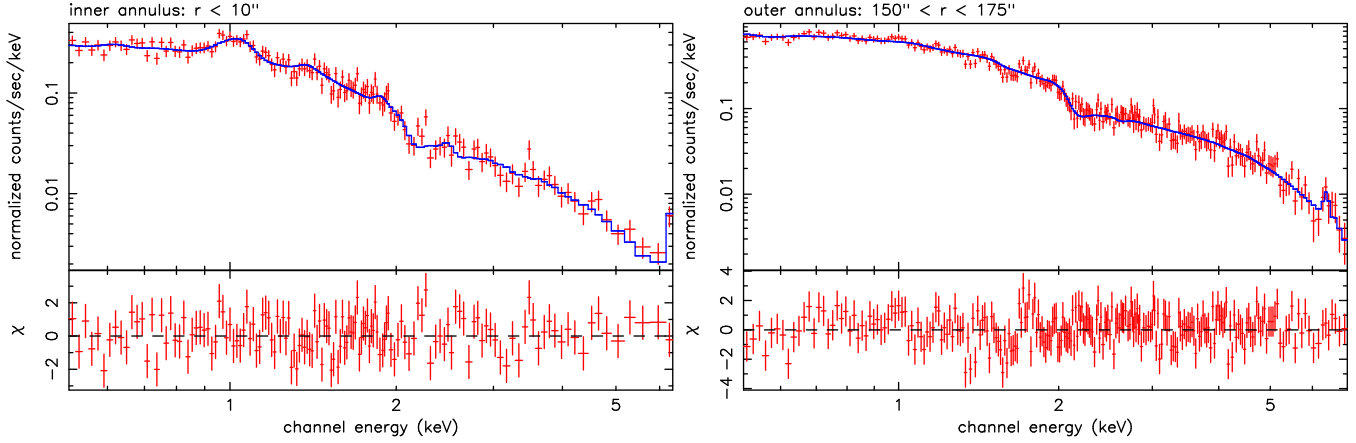


**Figure 6.** Observed spectra and best-fit absorbed MEKAL model for two representative annular regions.

**Table 2.** Results of the spectral analysis in annuli. In the second column, we quote the net count rate in the 0.5–7 keV energy range and, in parenthesis, the percentage of the total counts that are associated to the source. The models used are: *absIT* = *tbabs*(*mekal*) and *absCF* = *tbabs*(*mekal*+*ztbabs*(*cfmodel*)). The *absCF* has the column density fixed to the Galactic value of  $1.2 \times 10^{20} \text{ cm}^{-2}$ , whereas *absIT* considers  $N_{\text{H}}$  as free parameter.  $\dot{M}$  (in  $M_{\odot} \text{ yr}^{-1}$ ) and  $\Delta N_{\text{H}}$  (in  $10^{22} \text{ cm}^{-2}$ ) are integrated values from the circular region that includes all the inner annuli. The comparison between the null-hypothesis probability of the *absCF* model versus *absIT* is in Fig. 8. The metallicity refers to the solar photospheric values in Anders & Grevesse (1989).

Ann	Net cts rate	<i>absIT</i>			<i>absCF</i>				
" (kpc)	cts s <sup>-1</sup> (%)	<i>T</i> /keV	<i>Z</i> / <i>Z</i> <sub>⊙</sub>	χ <sup>2</sup> (d.o.f.)	<i>T</i> /keV	<i>Z</i> / <i>Z</i> <sub>⊙</sub>	$\dot{M}$	Δ <i>N</i> <sub>H</sub>	χ <sup>2</sup> (d.o.f.)
0–10 (0–17)	0.362±0.004 (99.9)	3.36 <sup>+0.12</sup> <sub>-0.12</sub>	0.63 <sup>+0.09</sup> <sub>-0.07</sub>	159.2 (141)	3.83 <sup>+0.16</sup> <sub>-0.33</sub>	0.75 <sup>+0.12</sup> <sub>-0.14</sub>	7.9 <sup>+2.4</sup> <sub>-2.5</sub>	0.18 <sup>+0.24</sup> <sub>-0.05</sub>	156.3 (140)
10–25 (17–41)	1.254±0.008 (99.8)	3.91 <sup>+0.11</sup> <sub>-0.10</sub>	0.56 <sup>+0.05</sup> <sub>-0.05</sub>	306.8 (241)	4.23 <sup>+0.09</sup> <sub>-0.10</sub>	0.60 <sup>+0.05</sup> <sub>-0.05</sub>	36.0 <sup>+7.4</sup> <sub>-7.9</sub>	0.25 <sup>+0.06</sup> <sub>-0.05</sub>	300.7 (240)
25–40 (41–66)	1.506±0.009 (99.7)	4.86 <sup>+0.12</sup> <sub>-0.10</sub>	0.71 <sup>+0.06</sup> <sub>-0.06</sub>	323.8 (275)	5.28 <sup>+0.15</sup> <sub>-0.14</sub>	0.75 <sup>+0.06</sup> <sub>-0.06</sub>	38.3 <sup>+6.5</sup> <sub>-6.3</sub>	0.12 <sup>+0.03</sup> <sub>-0.03</sub>	312.2 (274)
40–55 (66–91)	1.337±0.008 (99.6)	5.23 <sup>+0.15</sup> <sub>-0.23</sub>	0.43 <sup>+0.06</sup> <sub>-0.04</sub>	262.5 (262)	5.86 <sup>+0.19</sup> <sub>-0.17</sub>	0.45 <sup>+0.07</sup> <sub>-0.05</sub>	58.7 <sup>+8.8</sup> <sub>-7.7</sub>	0.12 <sup>+0.02</sup> <sub>-0.03</sub>	248.9 (261)
55–75 (91–124)	1.474±0.009 (99.3)	5.55 <sup>+0.17</sup> <sub>-0.13</sub>	0.38 <sup>+0.06</sup> <sub>-0.04</sub>	308.6 (281)	5.91 <sup>+0.19</sup> <sub>-0.15</sub>	0.40 <sup>+0.06</sup> <sub>-0.04</sub>	73.9 <sup>+9.5</sup> <sub>-8.5</sub>	0.11 <sup>+0.02</sup> <sub>-0.02</sub>	305.6 (280)
75–100 (124–165)	1.509±0.009 (98.8)	5.94 <sup>+0.15</sup> <sub>-0.17</sub>	0.44 <sup>+0.05</sup> <sub>-0.05</sub>	369.4 (290)	6.33 <sup>+0.15</sup> <sub>-0.29</sub>	0.46 <sup>+0.05</sup> <sub>-0.06</sub>	90.3 <sup>+9.1</sup> <sub>-10.5</sub>	0.11 <sup>+0.02</sup> <sub>-0.02</sub>	367.4 (289)
100–125 (165–206)	1.255±0.008 (98.1)	6.10 <sup>+0.21</sup> <sub>-0.12</sub>	0.37 <sup>+0.06</sup> <sub>-0.06</sub>	294.2 (274)	6.84 <sup>+0.39</sup> <sub>-0.37</sub>	0.38 <sup>+0.06</sup> <sub>-0.06</sub>	100.8 <sup>+13.4</sup> <sub>-11.8</sub>	0.12 <sup>+0.02</sup> <sub>-0.02</sub>	290.6 (273)
125–150 (206–248)	1.062±0.008 (97.4)	6.34 <sup>+0.25</sup> <sub>-0.20</sub>	0.35 <sup>+0.07</sup> <sub>-0.06</sub>	286.8 (258)	7.43 <sup>+0.55</sup> <sub>-0.45</sub>	0.39 <sup>+0.08</sup> <sub>-0.08</sub>	115.6 <sup>+12.1</sup> <sub>-9.5</sub>	0.11 <sup>+0.01</sup> <sub>-0.01</sub>	279.4 (257)
150–175 (248–289)	0.887±0.007 (96.3)	6.49 <sup>+0.43</sup> <sub>-0.39</sub>	0.18 <sup>+0.07</sup> <sub>-0.07</sub>	265.1 (239)	8.97 <sup>+0.87</sup> <sub>-0.94</sub>	0.23 <sup>+0.08</sup> <sub>-0.06</sub>	132.9 <sup>+11.6</sup> <sub>-11.6</sub>	0.10 <sup>+0.01</sup> <sub>-0.01</sub>	250.3 (238)

(hereafter *spectral deprojection*) and the surface brightness profile (*spatial deprojection*).

The deprojection analysis makes the assumption that the emission is spherically symmetric and the X-ray emitting plasma is in hydrostatic equilibrium with the underlying gravitational potential, which is likely to be reasonable on intermediate to larger scales considering that the sound crossing time in the inner 100 kpc is less than  $10^8$  years.

Considering that we are not able to distinguish between single phase and cooling flow models in the fitting analysis of our spectra as discussed in Section 4, we adopt hereafter for simplicity the single phase description to infer the properties of the intracluster medium.

### 5.1 Spectral deprojection

The physical quantities constrained from the projected spectra need to be translated to their 3-dimensional values to allow us to investigate the proper characteristics of the X-ray emitting plasma. Fitting a thermal model to a spectrum obtained collecting X-ray counts in rings provides, for each annulus, (i) an estimate for the Emission Integral,  $EI = \int n_e n_p dV = 0.82 \int n_e^2 dV$ , through the normalization  $K$  of the model,  $K = \frac{10^{-14}}{4\pi d_{\text{ang}}^2 (1+z)^2} EI$  (see MEKAL model in XSPEC); (ii) a direct measurement of the emission-weighted gas

temperature,  $T_{\text{ring}}$ , metal abundance,  $Z_{\text{ring}}$ , and luminosity,  $L_{\text{ring}}$ . The purpose of the deprojection is, for example, to recover the value of the gas temperature in shells,  $T_{\text{shell}} \equiv T_i$ , that is defined as

$$T_{\text{ring}} \equiv T_j = \frac{\sum_{i=j}^{i=j} T_i w_{ij}}{\sum_{i=j}^{i=j} w_{ij}} \quad (1)$$

where  $w_{ij} = L_i \times \text{Vol}(i, j) / \text{Vol}(i) = \epsilon_i \text{Vol}(i, j)$  provides the luminosity for a given shell  $i$  with volume  $\text{Vol}(i)$  weighted by the part of this volume projected on the ring  $j$ ,  $\text{Vol}(i, j)$ . Using this notation, it is simple to note that  $L_{\text{ring}} \equiv L_j = \sum_{i=j}^{i=j} \epsilon_i \text{Vol}(i, j) = \sum_{i=j}^{i=j} w_{ij}$ .

From Kriss, Cioffi & Canizares (1983; see also McLaughlin 1999), the volume of each shell observed through each ring adopted in the spectral analysis can be evaluated and a matrix, **Vol**, can be built with components equal to the parts the volume of the shells (rows  $i$ ) seen at each ring (or annuli; column  $j$ ).

The deprojected physical quantities can be then obtained through the following matrix products (shown by the symbol #):

$$\begin{aligned} n_e &= [(\mathbf{Vol}^T)^{-1} \# (EI/0.82)]^{1/2} \\ \epsilon &= (\mathbf{Vol}^T)^{-1} \# L_{\text{ring}} \\ \epsilon T_{\text{shell}} &= (\mathbf{Vol}^T)^{-1} \# (L_{\text{ring}} T_{\text{ring}}) \\ \epsilon Z_{\text{shell}} &= (\mathbf{Vol}^T)^{-1} \# (L_{\text{ring}} Z_{\text{ring}}), \end{aligned} \quad (2)$$

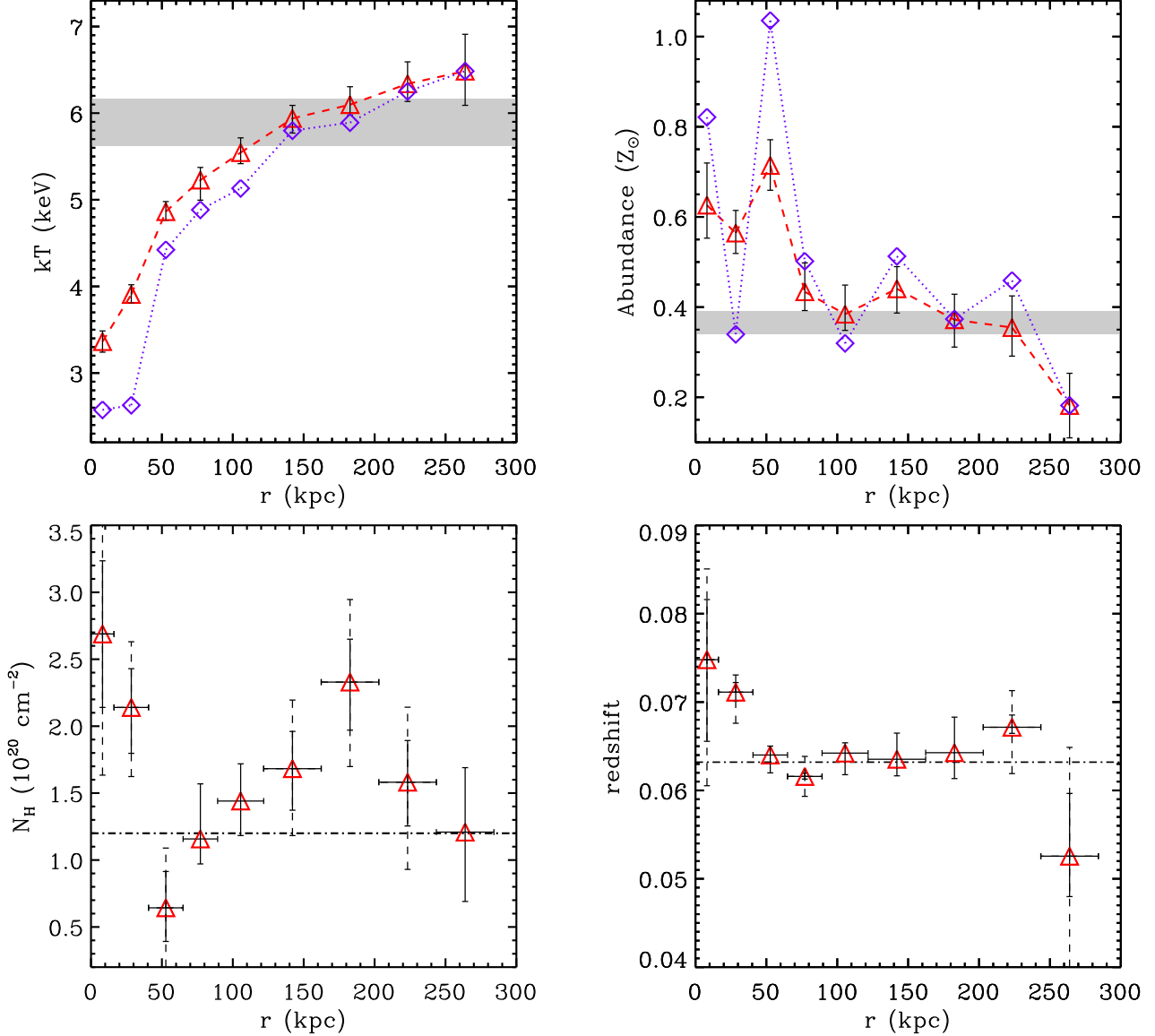


**Figure 7.** Best-fit spectral results applying a single absorbed MEKAL model (*triangles*; solar metallicity from Anders & Grevesse 1989) and the corresponding deprojected results (*diamonds*). The error bars are at  $1\sigma$  level. The shaded regions represent the uncertainties at the 90 per cent level of confidence from the ASCA analysis in Allen (2000). The dashed error bars refer to the 90 per cent confidence level ( $\Delta\chi^2 = 2.71$  on the interesting parameter). The dot-dashed lines indicate the Galactic absorption ( $N_{\text{H}} = 1.2 \times 10^{20} \text{ cm}^{-2}$ , Dickey & Lockman 1990) and the optical determination of the redshift at 0.0632 (Girardi et al. 1998), respectively.

where  $(\text{Vol}^T)^{-1}$  indicates that the matrix is firstly transposed and then inverted. The emission due to the shells projected along the line of sight but with the corresponding annuli outside the field-of-view is taken into account with an edge correction factor estimated assuming a power law distribution of the emission proportional to  $r^{-4}$  (cfr. equation A8 in the appendix of McLaughlin 1999).

We have applied this technique to the single-phase results of our spectral analysis (model *absIT* in Sect. 4). In rings where part of the flux was masked for the presence of a point-source, we correct the normalisation  $K$  by the relative amount of area not considered. (We note that, if we fit simultaneously the nine spectra with a combination of single phase models properly weighted with the correspondent volume of the shell observed at each ring, we mea-

sure a  $\chi^2$  of 2604.3 with 2278 degrees of freedom that is statistically undistinguishable from the sums of the results in Table 2 of  $\chi^2 = 2576.4$  and 2261 degrees of freedom).

The deprojected temperature gradient can then be compared with the output of the spatial deprojection code to constrain the gravitational potential and the mass deposition rate. The error bars come from 100 Monte-Carlo simulations obtained from scattering the original projected input with respect to their Gaussian error.

The deprojected gas temperature and metallicity are slightly steeper than the observed, projected profiles (cf. Fig. 7). The gas temperature rises from  $2.6^{+0.3}_{-0.5}$  to  $6.5^{+0.4}_{-0.3}$  keV at 270 kpc. The profile can be fitted ( $\chi^2=10.5$ , 7 d.o.f.,  $P=0.16$ ) with a power law:  $T_{\text{gas}} = 2.74^{+0.41}_{-0.23} \times (r/10\text{kpc})^{0.27(-0.06,+0.04)}$  keV. The metal

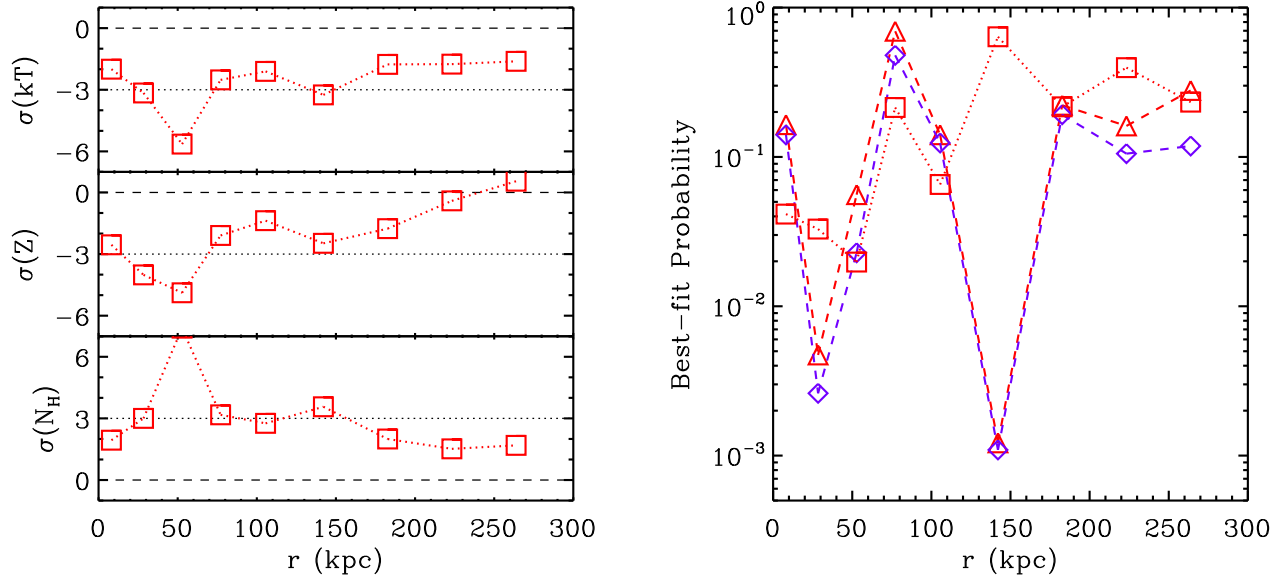


**Figure 8.** **Left panel** This panel shows the discrepancy (in  $\sigma$ ) between the best-fit results using the *absIT* model between the datasets with Focal Plane temperature of  $-110^\circ$  (calibration files of the December 1999 release) and  $-120^\circ$  (calibration files of the August 2001) currently used and plotted in Fig. 7:  $(data_{-110} - data_{-120}) / \sqrt{\sigma_{-110}^2 + \sigma_{-120}^2}$ . **Right panel** The null hypothesis probability of the best-fit results is shown for each annulus considered for the following *dataset/model*: “ $-120^\circ/absCF$ ” (triangles), “ $-120^\circ/absIT$ ” (diamonds), “ $-110^\circ/absIT$ ” (squares).

**Table 3.** Values of the minimum  $\chi^2$  (degrees of freedom in parenthesis) for each spectrum investigated in the present work for the following models: *absIT* = *tbabs*(*mekal*); *absITZ* = *tbabs*(*vmekal*); *absCF* = *tbabs*(*mekal*+*ztbabs*(*cfmodel*)). The column density in *absCF* is fixed to the Galactic value of  $1.2 \times 10^{20} \text{ cm}^{-2}$ , whereas the other models consider  $N_H$  as free parameter. The ratio  $F$  between the reduced  $\chi^2$  obtained from *absIT* and *absCF* is distributed as an F-distribution with  $m$  and  $n$  degrees of freedom, where  $m$  and  $n$  are equal to the d.o.f. in *absIT* and *absCF*, respectively (Bevington & Robinson 1992, pag. 205). The probability  $P$  that a random variable is larger than  $F$  is quoted with the required value,  $F_{95}$ , of  $F$  to obtain a level of significance of the 95 per cent. The null-hypothesis probabilities of the best-fit results obtained with *absCF*, *absIT* and *absITZ* are shown in Fig. 8 and Fig. 14.

Ann " (kpc)	<i>absIT</i>	<i>absITZ</i> $\chi^2$ (d.o.f.)	<i>absCF</i>	F test		
				$F$	$P$	$F_{95}$
0–10 (0–17)	159.2 (141)	153.1 (137)	156.3 (140)	1.01	0.47	1.32
10–25 (17–41)	306.8 (241)	300.1 (237)	300.7 (240)	1.02	0.45	1.24
25–40 (41–66)	323.8 (275)	318.2 (272)	312.2 (274)	1.03	0.39	1.22
40–55 (66–91)	262.5 (262)	249.2 (258)	248.9 (261)	1.05	0.34	1.23
55–75 (91–124)	308.6 (281)	306.3 (277)	305.6 (280)	1.01	0.48	1.22
75–100 (124–165)	369.4 (290)	354.8 (286)	367.4 (289)	1.00	0.49	1.21
100–125 (165–206)	294.2 (274)	285.8 (270)	290.6 (273)	1.01	0.47	1.22
125–150 (206–248)	286.8 (258)	279.0 (254)	279.4 (257)	1.02	0.43	1.23
150–175 (248–289)	265.1 (239)	252.4 (235)	250.3 (238)	1.05	0.34	1.24

(iron) abundance decreases from a central value of about 0.8 times the solar abundance to  $0.18(\pm 0.07)$ .

## 5.2 Spatial deprojection

To reach more firm conclusions on the state of the intracluster plasma in the inner region, we have combined the results of the spectral deprojection with the *spatial deprojection* of the X-ray surface brightness profile, which has been done applying the code developed from Fabian et al. (1981; see details on the code in White, Jones & Forman 1997). The surface brightness profile has been obtained in the 0.5–7 keV energy range with a bin-size of 9.8 arcsec (i.e. 20 times the original ACIS bin-size). Considering that the cluster emission covers the whole CCD, we have estimated a background count-rate of about  $1.5 \times 10^{-6} \text{ cts s}^{-1} \text{ arcsec}^{-2}$  from the blank-field used in the spectral analysis (Sect. 4). We detect signal

up to 4.4 arcmin ( $\sim 440 \text{ kpc}$ ) from the assigned centre with  $\gtrsim 5\sigma$  confidence.

The results from the spectral deprojection analysis are used to constrain the process of the spatial deprojection in the way described below (and similar to the procedure adopted in Allen, Etorri & Fabian 2001, Schmidt, Allen & Fabian 2001). In the spatial deprojection, there are 5 free parameters: (i) the column density,  $N_H$ , fixed to the averaged value observed in the spectral analysis of about  $1.6 \times 10^{20} \text{ cm}^{-2}$ ; (ii) the metallicity fixed to 0.3 times the solar value in accordance with the mean behaviour of the deprojected abundance profile; (iii) the outer pressure, fixed to the value of  $27.6 \times 10^4 \text{ K cm}^{-3}$ , extrapolated from the pressure profile estimated from the deprojected spectral temperature and gas density profiles; (iv-v) the scale (core) radius and the velocity dispersion describing the assumed potential law [in the present case either an isothermal sphere (Binney & Tremaine 1987, eqn. 4-124b) or

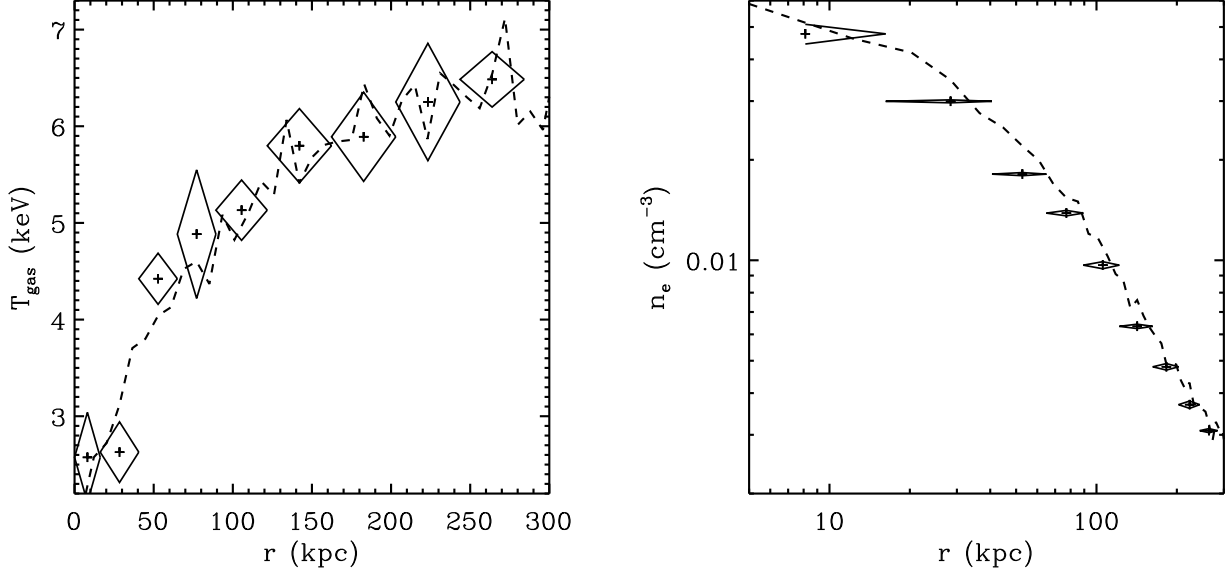


**Figure 9.** Comparison between the *spectral* (diamonds with error bars) and *spatial* (dashed line) deprojection results on the gas temperature (left panel) and electron density (right panel).

a Navarro, Frenk & White profile (NFW, 1997)]. The last two parameters are obtained from a  $\chi^2$  minimization between the gas temperature profile obtained from spectral deprojection of the single-phase analysis results (cf. Sect. 4) and the output of the spatial deprojection code properly rebinned (cf. eqn.1) to match the number of bins of the spectral profile. (In the spatial deprojection, the errors are obtained from the distribution of the results of the deprojection of 100 Monte-Carlo simulations of the original surface brightness profile.)

The best-fit between the two temperature profiles are obtained for the following values of the two free parameters of the potential laws:  $r_c = 0.10^{+0.01}_{-0.01}$  Mpc,  $\sigma_{\text{IS}} = \sqrt{(4/9)\pi G \rho_0 r_c^2} = 658^{+14}_{-11}$  km s $^{-1}$  for the isothermal sphere;  $r_s = 0.49^{+0.11}_{-0.13}$  Mpc,  $\sigma_{\text{NFW}} = \sqrt{(GM_{200})/(2r_{200})} = \sqrt{50} H_0 r_{200} = 837^{+69}_{-85}$  km s $^{-1}$  when a NFW potential law is assumed. Note that  $\rho_0$  and  $r_c$  define the central matter density and the core radius, respectively, in the isothermal sphere, whereas  $M_{200}$  indicates the total mass within the radius  $r_{200}$  where an overdensity of 200 with respect to the background is reached. Note also that the two velocity dispersions are related by the equation  $2\sigma_{\text{NFW}}^2 = (-d \ln \rho / d \ln r) \sigma_{\text{IS}}^2$  (cf. eqn.4-127b in Binney & Tremaine 1987) and tend to be equal when regions extending at  $r \gtrsim 10r_c$  can be considered (see Figure 4-8 in Binney & Tremaine 1987; in our case, we are mapping regions within  $\sim 4r_c$ ). However, we observe a lower  $\chi^2$  for a potential with a flat profile in the core, namely  $\chi^2 = 7.1$  (with 7 degrees of freedom,  $P=0.41$ ) for the isothermal sphere against 16.5 ( $P=0.02$ ) for a NFW profile.

In Fig. 9, we show the gas temperature and density profiles from the spectral deprojection analysis compared to those obtained from the best-fit results in the spatial deprojection. It is worth noting that the good agreement between the two gas density profiles is due to the dominance of the density in the X-ray emissivity that allows an almost temperature-independent deprojection, whereas we have required that the two temperature profiles match, searching for a minimum  $\chi^2$  in comparing these profiles with the parameters of the gravitational potential left free to vary. Moreover, this comparison

shows the self-consistency of our results and provides us with a cooling time and a mass deposition rate profiles with resolution of the imaging data (see discussion in Section 5.5).

### 5.3 Cluster mass profile in the core

In our spectral analysis, we are able to resolve in 5 radial bins the gas temperature profile in the inner 100 kpc radius with a relative uncertainty less than 5 (10) per cent for the projected (deprojected) temperature. This enables us to investigate the mass profile in the cluster core assuming that the intracluster medium is there in hydrostatic equilibrium with the dark matter potential.

We make use of the gas temperature and electron density values estimated from the deprojected best-fit spectral results obtained with a single-phase model (see Section 5.1). Then, we apply the equation of hydrostatic equilibrium between the gravitational potential and the intracluster plasma to estimate the mass profile,  $M_X$ ,

$$M_X = - \frac{Tr^2}{G\mu m_p} \left( \frac{d \ln T + d \ln n}{dr} \right). \quad (3)$$

In doing this, we interpolate the gas temperature profile with a polynomial of 2nd order to smooth over any fluctuations for the results from spectral deprojection. Moreover, we estimate the mass profile using a smoothed temperature and density profiles obtained from the best-fit results of the spatial deprojection (see Section 5.2). We assume a relative error propagated from the results of the spectral deprojection of about 15 per cent consistent with 1.5 times the uncertainty on the gas temperature measurements. In Fig. 10, we compare these dark matter profiles with the best-fit results obtained fitting the outer region of the cluster emission observed with *Rosat* PSPC (for details see Ettori & Fabian 1999) both with a  $\beta$ -model (Cavaliere & Fusco-Femiano 1976;  $r_c = 0.25$  Mpc,  $\beta = 0.75$ ) and a gas model obtained from the NFW potential law ( $r_s = 0.77$  Mpc,  $\eta = 10.70$ ).

To assess the shape of the underlying gravitational potential in

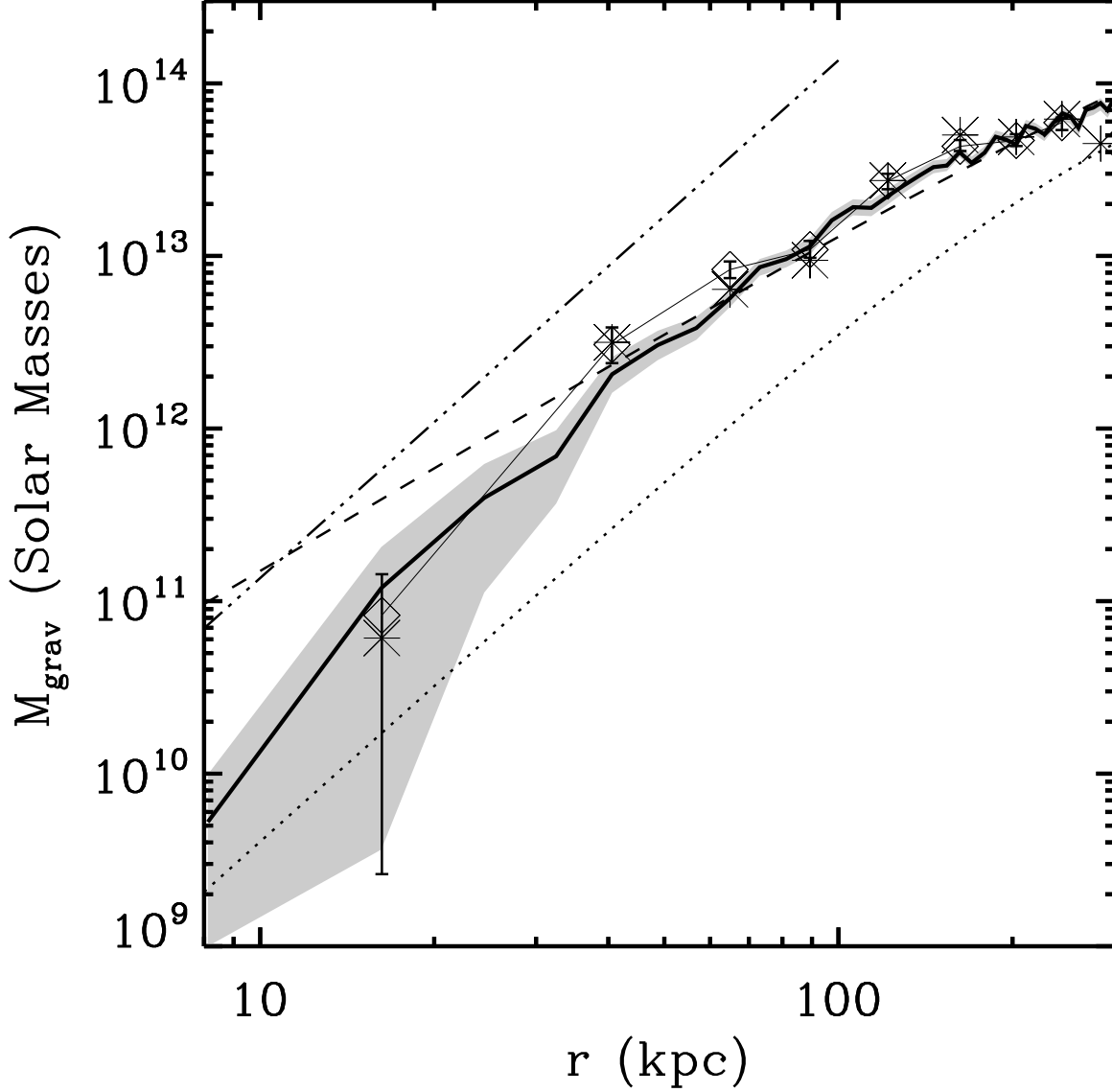


**Figure 10.** Gravitational mass profiles. The solid line is the mass profile obtained through the hydrostatic equilibrium equation applied to the results from the spatial deprojection on the gas temperature and density profiles (see Sect. 5.2 for details). The *diamonds* are the total mass values obtained using the deprojected spectral temperature and density measures. The *asterisks* are the total mass values obtained from the spectral deprojection when the X-ray center is fixed on the cD galaxy. These values are compared with the best-fit results on *Rosat* PSPC data (Ettori & Fabian 1999) using a  $\beta$ -model (dotted line) and a gas NFW model (dashed line). The three-dots-dash line indicates the upper limit from an assumed tidal shear in the  $H_\alpha$  filament due to the central cluster potential.

the central region, we describe the dark matter profile with a power law expression,  $\rho_{\text{grav}} = \rho_0(r/r_0)^{-\alpha}$ , integrate it over the volume

$$M_{\text{grav}} = \int_0^R 4\pi \rho_{\text{grav}} r^2 dr = \frac{4\pi \rho_0 r_0^3}{3-\alpha} \left(\frac{R}{r_0}\right)^{3-\alpha} \quad (4)$$

and fit this mass profile to the one from the spectral deprojection results (see Fig. 10) between 10 and 100 kpc, where the discrepancy among the different forms of the potential is more significant. We measure  $\alpha = 0.59^{+0.12}_{-0.17}$  (in the range 0.27–0.81 at the 90 per cent confidence level; Fig. 11), that indicates a remarkable flat profile

suggesting the presence of a core. In particular, a value of 1 (typical for cuspy dark matter profile like NFW) is excluded at more than  $3\sigma$ . In other words, we expect four times more than the observed mass in the inner bin, if we assume a power law index of 1 and a fixed mass at 100 kpc. On the other hand, the deviation from a flat core (i.e.  $\alpha = 0$ ) makes the mass profile lie apart from that expected given a King profile. The presence of this “shoulder” has been detected also by Xu et al. (1998) from *ASCA* and *Rosat* PSPC data and is now resolved with *Chandra*. Finally, from the presence of a shear in the  $H_\alpha$  filament southward the cD galaxy, Hu, Cowie

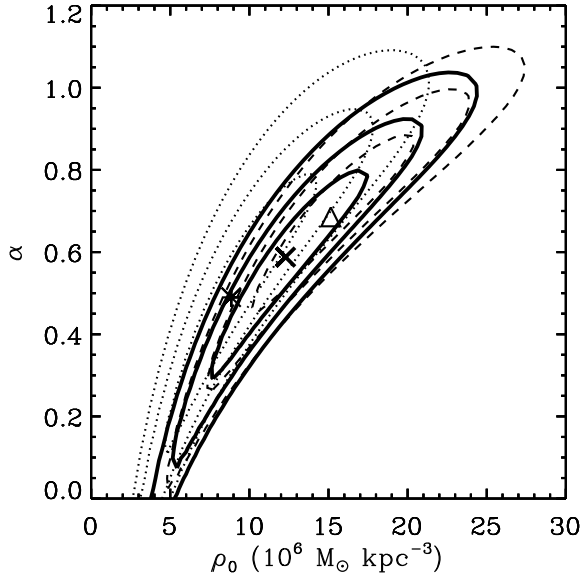


**Figure 11.** Contours of the probability distribution ( $\Delta\chi^2 = 2.3, 6.2, 11.8$  that correspond to 1, 2, 3  $\sigma$  for two interesting parameters) using the power-law model in eqn. 4 on the mass profile from spectral deprojection results (diamonds in Fig. 10) between 10 and 100 kpc (solid line and cross). The dotted line (asterisk) is for the mass profile from X-ray analysis centered on the cD galaxy. The dashed lines (triangle) indicate the confidence levels when the mass is increased by 40 per cent in the inner two bins only.

and Wang (1985) conclude that the central gravitational potential is not too deep. Following their arguments on the tidal shearing of the filament in the cluster potential, we obtain an upper limit on the central mass (assuming constant density) consistent with our results and that excludes any dark matter density profile sharper than the NFW form below 10 kpc (see Fig. 10).

It is worth noticing that this result is not function of the X-ray center adopted in our analysis (see discussion in Section 3). As shown in Fig. 10, moving the center of the circular annuli used to collect the spectra to the cD galaxy does not change the mass profile. Moreover, the presence of a multi-phase gas could affect our estimate of the gravitational potential. Gunn & Thomas (1996) show that, given the same emissivity, the single phase assumption underestimates the total mass by 20–40 per cent. Considering that the evidence for a truly multi-phase gas is weak and the gas is not certainly described from a steady-state cooling flow model (see, e.g., the discrepancy between the deposition rate obtained from spatial and spectral deprojection in Section 5.5), the correction factors for A1795 would be smaller than these. Adopting these upper limits and increasing by 40 per cent the mass values in the two inner bins do not change the results significantly (cf. Fig. 11).

#### 5.4 On the dynamical state of the core

The analysis of the surface brightness distribution in Section 3 suggests that the intracluster medium has an unrelaxed nature that might introduce a kinetic pressure component in the hydrostatic equilibrium equation so raising the total effective mass in the central core. This could possibly explain the flattening of the gravitating mass profile. Assuming that underlying potential is described from NFW and  $\Delta M$  is the difference with respect to the observed

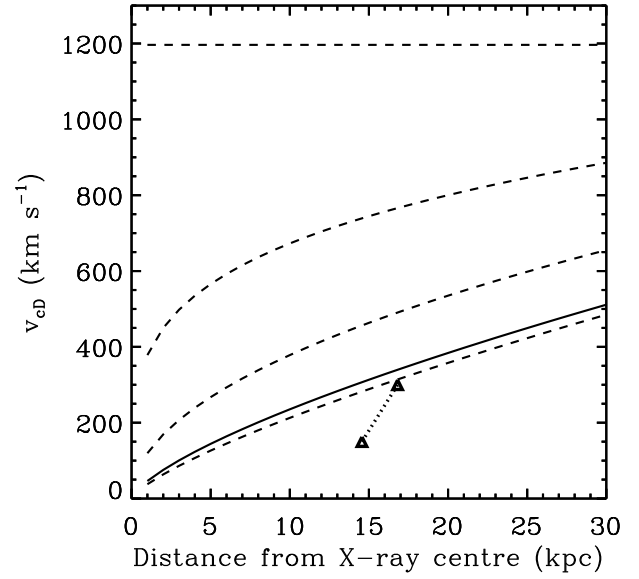


**Figure 12.** Predicted velocity of the cD galaxy under the effect of different gravitational potentials as a function of the separation from the X-ray centre assumed to be consistent with the deepest point of the potential well. The solid line indicates the estimated potential and the dashed lines are for dark matter density profiles with power law index of  $-0.5$ ,  $-1$  (as in NFW),  $-1.5$  (as in Moore et al., 1999) and  $-2$  upwards, respectively. The dotted line shows the range of the values in the velocity–separation space for angles with respect the line-of-sight between 0 and 60 degrees. At  $0^\circ$ , these values correspond to the observed peculiar velocity of  $150 \text{ km s}^{-1}$  and measured separation between cD galaxy and assumed X-ray centre of about 9 arcsec.

mass estimates, a bulk motion with velocity (assumed independent from radial position) of  $\sim 300 \text{ km s}^{-1}$  is required from the equation  $d(v^2 \rho_{\text{gas}})/dr = -(G \rho_{\text{gas}} \Delta M)/r^2$ . This value is lower than the gas sound speed of about  $800 \text{ km s}^{-1}$  and definitely subsonic.

It is worth noting that the shape of the gravitational potential is consistent with the detected motion of the cD galaxy. Oegerle & Hill (1994) measure a cD velocity redshifted relative to the cluster of  $\sim 150 \text{ km s}^{-1}$ . The emission-line velocity map in Hu et al. (1985) shows that the H $\alpha$ /X-ray filament has the same velocity of the cluster and is blueshifted from the cD velocity by still  $150 \text{ km s}^{-1}$  (from recent H $\alpha$  observation, this can be considered as an upper limit; C. Crawford, priv. comm.). In Fig. 12, the cD velocity is estimated as  $v_{\text{cD}} = (2GM_{\text{grav}}/r)^{0.5}$ , where  $G$  is the gravitational constant and  $M_{\text{grav}}$  is the total gravitating mass within the radius  $r$  calculated from eq. 4. Fixing the gravitational mass at  $r = 100 \text{ kpc}$ , we can change the power law index  $\alpha$  and investigate the behaviour of the cD velocity. As shown in Fig. 12, a cD velocity larger than  $400 \text{ km s}^{-1}$  is required for potential well described by a dark matter density profile steeper than  $r^{-1}$ . Given the observed velocity offset along the line of sight, the presence of a density profile flatter than a NFW profile is then required.

If we model the motion of the dominant galaxy as an harmonic oscillation at the bottom of the potential well (e.g. Lazzati & Chincharini 1998), we assume that the cD galaxy passed through the X-ray cluster centroid at the time zero with maximal velocity and, then, underwent an oscillatory motion described from the equations,  $x_{\text{cD}} = A \cos(\omega t + \phi)$ ,  $v_{\text{cD}} = -A\omega \sin(\omega t + \phi)$ , where the phase  $\phi = -\pi/2$  and  $\omega = (GM_{\text{grav}}/r^3)^{0.5} \approx 5 \times 10^{-16}$ . Solv-

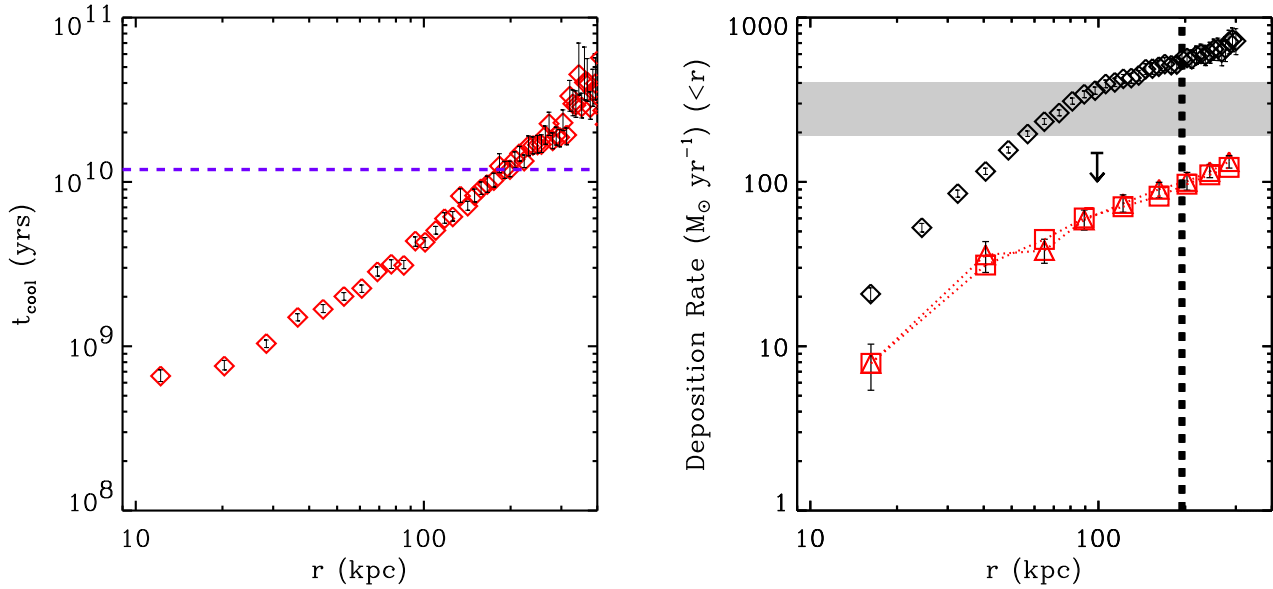


**Figure 13.** (Left) *Spatial* deprojection results on the cooling time. The dashed line indicates the age of the universe at the cluster redshift,  $t_{\text{H}_0}$ . Within 10 kpc radius, the cooling time is about  $3.4 \times 10^8$  yrs. (Right) *Spatial* (diamonds) and *spectral* (triangles: from concentric rings; squares: from annuli) deprojection results on the integrated deposition rate,  $\dot{M}(<r)$ . The RGS-XMM upper limit is indicated by the downward arrow. The vertical dashed line corresponds to the radius of 191 kpc where  $t_{\text{cool}} = t_{\text{H}_0}$ . The dashed region shows the 90 per cent confidence level from ASCA analysis (Allen et al. 2001).

ing the above two equations, we find that the cD galaxy crossed the centroid about  $1.3 \times 10^8$  years ago with velocity of  $\sim 400 \text{ km s}^{-1}$ . Considering our interpretation of the X-ray filament pointing southward as a cooling wake (see Fabian et al. 2001b for a discussion), we can use this age as an upper limit on the cooling time of the densest, coolest phases in the central plasma.

### 5.5 On the cooling flow model

As discussed in Section 4, we cannot conclude that the gas in the core of A1795 is multi-phase. However, this gas would cool radiatively in about  $10^9$  years ( $3.8 \times 10^8$  yrs in the central 10 kpc radius, with 10th and 90th percentile of 3.2 and  $4.4 \times 10^8$  yrs, respectively), approaching the estimated age of the Universe at the cluster redshift of  $1.2 \times 10^{10}$  years at about 200 kpc (Fig. 13). This can be considered as an upper limit on the region where cooling is taking place. In particular, the physical extension of the central region, where a X-ray soft component dominates the emission, can be obtained from the X-ray colour profile shown in Fig. 5, where the profile flattens at about 100 kpc. This is consistent with the break observed in the  $\dot{M}(r)$  profile discussed below and presented in Fig. 13.

To maintain the cluster core in pressure equilibrium as energy is lost to radiation, and if there is not balancing from any heating sources, a flow of material occurs inward and deposition of cool gas mass takes place in the central region of the cluster. In this *cooling flow* scenario (e.g. Fabian 1994), the amount of gas deposited within a given radius,  $\dot{M}(<r)$ , can be estimated and used to parametrize the luminosity originating from the cooling materials. We measure  $\dot{M}(<r)$  in two ways (Fig. 13): in the *spatial deprojection*, it is provided from the luminosity associated to the gas that either (i) cools completely in a shell or (ii) passes the shell changing temperature under the action of the cluster potential (cf. White, Jones & Forman 1997); in the *spectral analysis*,  $\dot{M}(<r)$

is estimated as the amount of gas that cools from the ambient temperature to zero through the modelling of the spectra accumulated in concentric circular region with a multi-phase model (Johnstone et al. 1992) absorbed by a column density intrinsic to the galaxy cluster that is required to reproduce properly the soft part of the spectra.

The cumulative values of  $\dot{M}(<r)$  obtained in the present analysis (Fig. 13) enclose the constraints available from the ASCA analysis in Allen et al. (2001), where no spatial resolution of  $\dot{M}(<r)$  was possible. The deviation between the spatial and spectral results on the  $\dot{M}$  profile, apart from the central two bins where the assumed spherical geometry is probably inappropriate given the observed cooling wake, is due to limitations on the validity of the steady-state cooling flow model. The dynamical scenario in which cooling flows establish and evolve considers merging with infalling substructures that interrupt the subsonic flow of material. These mergers are been shown to be responsible for several features in the surface brightness and temperature distribution (see, e.g., Markevitch et al. 2001, Vikhlinin et al. 2001, Mazzotta et al. 2001) and can be energetically relevant, thus throwing into question the assumption of steady-state mass accretion underlying the standard cooling flow model (e.g. Nulsen 1986). Therefore, we adopt hereafter the spectral estimates of the mass deposition rate as more reliable and use these as reference values.

Recent analysis of *XMM-Newton* data of A1795 (Tamura et al. 2001, Molendi & Pizzolato 2001) does not show detectable emission from gas cooling below 1–2 keV. Our lower limit from the deprojection of the best-fit gas temperature in the central 20 kpc radius is 1.8 keV at 90 per cent confidence level. When an isobaric cooling flow component is considered to model the *XMM-Newton* Reflection Grating Spectrometers (RGS) spectra of the central region, an upper limit (90 per cent level of confidence) of  $150 M_{\odot} \text{ yr}^{-1}$  is obtained (Tamura et al. 2001; note that these authors estimate that about 80 per cent of the emission observed in the RGS

spectra comes from regions enclosed within  $\sim 60''$ ). This value is larger than our value of  $74 M_{\odot} \text{ yr}^{-1}$  (90 per cent confidence limit of  $89 M_{\odot} \text{ yr}^{-1}$ ) measured within 75 arcsec from the X-ray centre. The *Chandra*-determined cooling flow therefore appears to be consistent with the present *XMM-Newton* RGS constraint. Within the central 200 kpc, we estimate a deposition rate of about  $100 M_{\odot} \text{ yr}^{-1}$  ( $< 121 M_{\odot} \text{ yr}^{-1}$  at 90 per cent c.l.), consistent with the early *ASCA* result of Fabian et al. (1994b) and lower than the estimate in Allen et al. (2001), where the assumption of an isothermal gas in the core (due to the limited spatial resolution of *ASCA*) causes an overestimate of the integrated deposition rate (up to a factor of  $\sim 3$  in the case of A2390 discussed in Allen, Etti & Fabian 2001). When a cooling flow model with a low temperature cut-off is considered (e.g. Tamura et al. 2001), good fits can be obtained for the inner 3 annuli with lower estimates of  $T_{\text{cut-off}} \sim 1.4 \text{ keV}$ . With respect to *absCF*, this model preserves the same number of degrees-of-freedom and provides a better  $\chi^2$  just for the second annulus that encloses a region between 10 and 25 arcsec ( $\Delta\chi^2 = -0.7, 3.3, -0.8$  for the inner three annuli, respectively, when compared with the results in Table 2). This is qualitatively in agreement with the results from *XMM-Newton* EPIC analysis in Molendi & Pizzolato (2001).

Note that we model the cluster emission with *absCF*, in which the cool emission is suppressed with an intrinsic absorption of about  $10^{21} \text{ particle cm}^{-2}$ . If we adopt the same model that describes the RGS spectra and consider a region of 75 arcsec radius (80 per cent of the emission observed in the RGS spectra comes from a projected radius of about 60 arcsec), fixing the outer thermal component to 6.4 keV with metallicity of 0.4 solar and the Galactic column density to  $3 \times 10^{20} \text{ cm}^{-2}$ , and not including any intrinsic absorption, we measure a normalization for the cooling flow component of  $140 M_{\odot} \text{ yr}^{-1}$  (90 per cent confidence limit range of  $133\text{--}152 M_{\odot} \text{ yr}^{-1}$ ) with a considerably worst  $\chi^2$  of 654 (387 d.o.f.) with respect to 535 (384) obtained with *absCF*. On the other hand, a cooling flow model with a low temperature cut-off provides a better fit ( $\chi^2 = 505, 383 \text{ d.o.f.}$ ; F-test probability of  $3 \times 10^{-3}$ ) with  $T_{\text{cut-off}} \approx 1.4 \text{ keV}$  (in the range 1.3–1.6 keV at 90 per cent c.l.) and normalization  $\dot{M} \approx 324 M_{\odot} \text{ yr}^{-1}$  (range at the 90 per cent c.l.:  $271\text{--}469 M_{\odot} \text{ yr}^{-1}$ ). The intrinsic absorption discussed above can be interpreted as one method to suppress the line emission from gas below  $\sim 1.5 \text{ keV}$ . Other methods and related issues are discussed by Peterson et al. (2001) and Fabian et al. (2001a).

## 5.6 Distribution of the metals

The X-ray emitting plasma is about 5 times more massive than the stars in galaxies (David et al. 1990, White et al. 1993) and, thus, is the major reserve of both baryons and heavy metals contained in galaxy clusters, since the Iron abundance is typically between 0.3 and 0.5 times the solar value (Mushotzky & Loewenstein 1997). Studies on the correlation between Fe mass and light coming from E and S0 galaxies (Arnaud et al. 1992, Renzini 1997) conclude that larger amount of iron resides in the intracluster medium than inside galaxies and its enrichment originated through releases from early-type galaxies.

The processes that preferably enrich the plasma are (i) (proto)galactic winds (De Young 1978, Metzler & Evrard 1994), that occur at early times and are characterized from supernova (SN) type II ejecta with large abundance of  $\alpha$  elements, and (ii) ram pressure stripping (Gunn & Gott 1972), that takes place on longer time scales due to the continuous accretion of fields galaxies in the cluster potential well and produces mostly SN Ia ejecta. A negative gra-

dient in the metallicity profiles is observed preferentially in cooling flow clusters (Allen & Fabian 1998, Irwin & Bregman 2001, De Grandi & Molendi 2001) and can be explained as enrichment of the inflowing gas by SNe Ia and stellar mass loss in the outer parts of the central dominant galaxy (Reisenegger, Miralda-Escudé & Waxman 1996).

What discriminates between these two main processes is the different elemental mass yields: SN Ia ejecta tend to be rich in Ni, whereas SN II ejecta present larger ratio between  $\alpha$  elements (e.g., O, Mg, Ar, Ca, S, Si) and Fe. Recent evidence of iron gradients in cluster cores with decreasing ratio between  $\alpha$  elements and Fe moving inward suggest that, while the global intracluster metal abundances are consistent with SN II ejecta (Mushotzky & Loewenstein 1997), SN Ia productions are dominant in the central cluster regions (Ishimaru & Arimoto 1997, Fukuzawa et al. 1998, Finoguenov, David & Ponman 2000, Allen et al. 2001, Dupke & Arnaud 2001).

To resolve and quantify the contribution from the single heavy elements, we fit the annular spectra with an absorbed VMEKAL model (*absITZ* in Table 3) using the solar elemental abundances from Grevesse & Sauval (1998) that update the commonly-used values in Anders & Grevesse (1989; note that the results on the azimuthally-averaged metallicity in Table 2 and Fig. 7 refer at these values for a direct comparison with previous work) and differ from these mainly in the abundance of Iron, Oxygen and Sulphur by a factor of 0.68, 0.79 and 1.32, respectively. We fix Helium to the cosmic abundance value and consider 5 groups of metals: O, C, N, Na, Mg and Al tied together; Ne; Si; S; Fe tied with Ca, Ar and Ni. In Fig. 14, we show the profiles for Ne, Si, S and Fe. We omit to plot the constraints on the value of the O abundance that is approximately flat around 0.4 times solar. In general, these fits show a null-hypothesis probability higher than the corresponding single abundance fit (right panel in Fig. 14).

To estimate the Fe mass fraction originated from SN Ia and SN II ejecta, we perform a  $\chi^2$  minimization at each radial bin of the merit function

$$\chi^2 = \sum_i \frac{(\text{ratio}_i - \text{mod}_i)^2}{\text{err}_i^2} \quad (5)$$

where  $\text{ratio}_i = [\text{O/Fe}, \text{Ne/Fe}, \text{S/Fe}, \text{Si/Fe}]$ ,  $\text{err}_i$  is the  $1 \sigma$  error on  $\text{ratio}_i$  propagated from the uncertainties in the fit and  $\text{mod}$  is equal to  $f \times \text{ratio}_{\text{SN Ia}} + (1 - f) \times \text{ratio}_{\text{SN II}}$ . The elemental abundance ratios for SN Ia (0.037, 0.006, 0.585, 0.538 for O/Fe, Ne/Fe, S/Fe, Si/Fe, respectively) and SN II (3.82, 2.69, 2.29, 3.53) yields are from Nomoto et al. (1997a, 1997b; for SN Ia yields, we refer to deflagration model, W7) and summarized in Table 4 in Dupke & Arnaud (2001). The radial profile of  $f_{\text{SN Ia}}$  is plotted at the bottom of the left panel in Fig. 14. The fraction in number of the SNe Ia is above 65 per cent everywhere within 200 kpc.

This is consistent with the higher null-hypothesis probability that we observe when the abundance ratios are fixed to the SN Ia production values instead of SN II values (right panel in Fig. 14).

A supernova produces  $0.74 M_{\odot}$  of iron when Type Ia (Thielemann, Nomoto & Hashimoto 1996),  $\sim 0.12 M_{\odot}$  when Type II (Gibson, Loewenstein & Mushotzky 1997). These values imply a total iron mass of  $M_{\text{Fe}} = 0.74 f_{\text{SN Ia}} N_{\text{SN Ia}} + 0.12(1 - f_{\text{SN Ia}}) N_{\text{SN II}}$ , where  $N_{\text{SN Ia}}$  and  $N_{\text{SN II}}$  are the number of SN Ia and SN II, respectively, and are estimated comparing this calculation of the iron mass with what measured from the observed iron abundance,  $Z_{\text{Fe}}$ , plotted in Fig. 7. In the latter case,  $M_{\text{Fe}} = A_{\text{Fe}} y_{\text{Fe}, \odot} Z_{\text{Fe}} M_{\text{H}}$ , where  $A_{\text{Fe}} = 55.8$ ,  $y_{\text{Fe}, \odot} = 3.16 \times 10^{-5}$  from Grevesse & Sauval (1998) and  $M_{\text{H}} = M_{\text{gas}}/1.33$  (we are

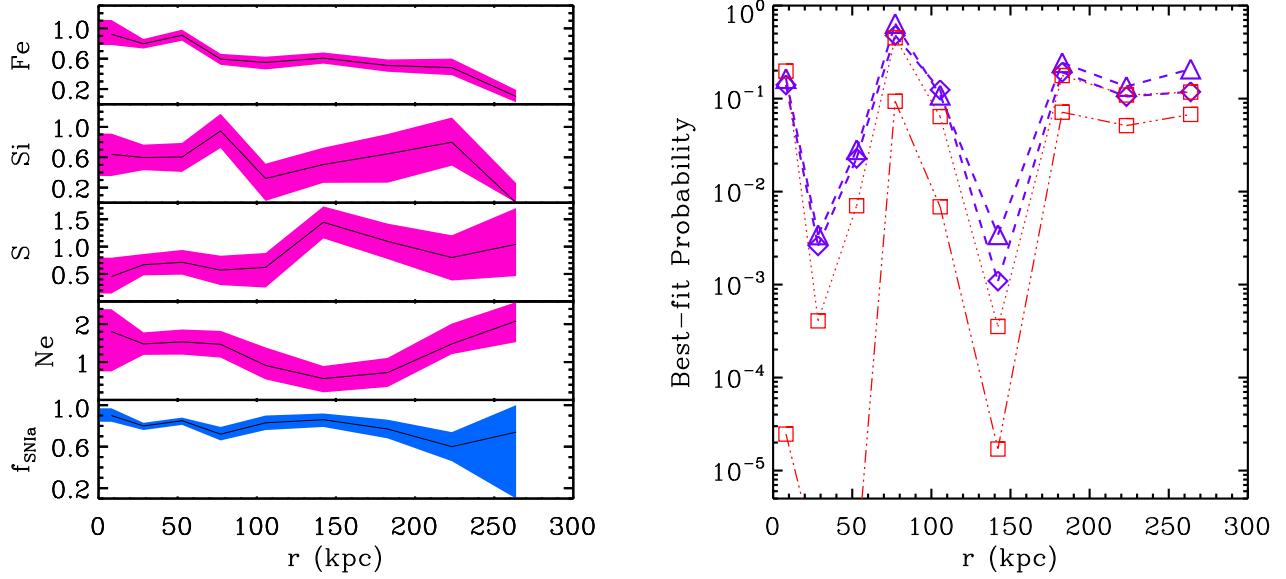


**Figure 14.** (Left) Abundance respect to the solar value of Fe, Si, S, Ne. The O profile is approximately flat around 0.4. The solar elemental abundance is from Grevesse & Sauval (1998). (Note that the results on the azimuthally-averaged metallicity in Table 2 and Fig. 7 refer at Anders & Grevesse (1989) for a direct comparison with previous work.) The bottom panel provides the fraction of SNIa that are aspected to contribute to the enrichment of the intracluster medium. (Right) Best-fit Null Hypothesis after using single abundance (MEKAL, diamonds), multi-abundances (VMEKAL, triangles), SNIa metals ratio (squares and dotted line), SNIi metals ratio (squares and dash-three-dot line).

assuming  $\mu = 0.6$ ,  $n_e = 1.21n_p$ ), and rises with radius from  $3 \times 10^7 M_\odot$  in the inner 10 kpc up to few times  $10^9 M_\odot$  at  $r > 100$  kpc. From the compilation on the rates of SNe Type Ia and II in Madau, Della Valle & Panagia (1998), a conversion factor between 1 and 5 is obtained from  $N_{\text{SNIi}}$  to  $N_{\text{SNIa}}$ . Using a central value of 3.5 (see also Iwamoto et al. 1999), we require a number of SN II that ranges between  $10^8$  and  $4 \times 10^{10}$  moving outward.

The amount of the total iron produced in SNIa is then  $M_{\text{Fe,SNIa}}/M_{\text{Fe}} \approx [1 + 3.5 \times (0.12/0.74) \times (f_{\text{SNIa}}^{-1} - 1)]^{-1} \approx (0.8 - 1)$  in the central 200 kpc.

Assuming that about  $80 M_\odot$  of star formation are required to generate a supernova Type II (e.g. Thomas & Fabian 1990), we conclude that the cumulative star formation that took place during the cluster history is  $\sim 0.7 - 2 \times 10^{12} M_\odot$  within the central 100-200 kpc, consistent with the expected amount of gas deposited during the existence of the cooling flow. From the  $H_\alpha$  luminosity of about  $10^{42} \text{ erg s}^{-1}$  coming from the central 12 kpc radius (Cowie et al. 1983), we infer a present star formation rate (SFR) of about  $9 M_\odot \text{ yr}^{-1}$  [Kennicutt 1983; Crawford et al. (1999) indicate a visible SFR of about  $2 M_\odot \text{ yr}^{-1}$  within 5 kpc-radius from optical observation of the central dominant galaxy], that has to be compared with an inferred cumulative value of about  $9 \times 10^9 M_\odot$  on the same region in exam. These values can agree with constant star formation rate over the last Gyr.

The deposition of material, star formation activity and residuals in form of absorbing dust (as suggested for central regions of cooling flow clusters; e.g. Voit & Donahue 1995, Fabian et al. 1994a, Allen 2000) can (i) explain the observed excess in the column density measurements in the inner 50 kpc of about 2 with respect to the Galactic value interpolated from radio maps, and (ii) be responsible for emerging reprocessed emission in the far infrared. From IRAS scans over the central 4 arcmin of A1795, Allen et al. (2001) infer a far-infrared luminosity of  $< 3.3 \times 10^{44} \text{ erg s}^{-1}$ , that

puts an upper limit on the present SFR of  $15 M_\odot \text{ yr}^{-1}$  (from relation in Kennicutt 1998), in agreement with the previous estimates.

Finally, this star formation activity releases energy during supernova explosions providing an amount of thermal energy per gas particle,  $E$

$$E = \frac{\eta E_{\text{SN}} N_{\text{SNIi}}}{M_{\text{gas}}/(\mu m_p)} \approx 0.4 \left( \frac{\eta}{0.1} \right) \left( \frac{N_{\text{SNIi}}}{10^{10}} \right) \left( \frac{10^{12} M_\odot}{M_{\text{gas}}} \right) \text{ keV}, (6)$$

where a kinetic energy release by one SN,  $E_{\text{SN}}$ , of about  $1.3 \times 10^{51} \text{ erg}$  (e.g. Iwamoto et al. 1999), a factor  $\eta$  that represents the efficiency of this kinetic energy in heating the ICM through galactic winds (and assumed here equal to 10 per cent) and typical values for the inner part of A1795 are adopted. When we compare  $E$  to the thermal energy per particle measured (cf. Fig. 7), we conclude that processes from SNe explosions are responsible for about 8 per cent of that energy.

## 6 SUMMARY AND CONCLUSIONS

The entropy of the gas increases monotonically moving outwards almost proportionally to the radius, with a best-fit  $\log(K) = -0.09 + 0.97 \log(r)$  (see Fig. 15). This behaviour traces the shock heating (more significant at larger radius) at which the intracluster gas has been subjected during its history of accretion in the gravitational potential well, whereas the efficiency of the cooling has removed the central gas at lower entropy (cf. Tozzi & Norman 2001).

Together with the estimated cooling time due to energy loss by radiation of less than  $10^9$  years and a decrease by a factor of 3 in the gas temperature, this seems to indicate that the central 200 kpc are undergoing significant cooling with a gas mass deposition rate of about  $100 M_\odot \text{ yr}^{-1}$  in the absence of any heating process.

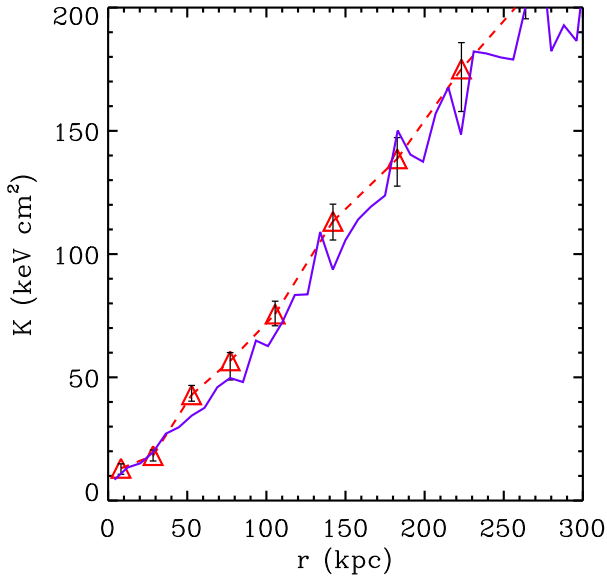


**Figure 15.** Comparison between the *spectral* (triangles) and *spatial* (solid line) deprojection results on the entropy,  $K = T_{\text{gas}}/n_{\text{gas}}^{2/3}$ , of the cluster gas.

This would require an intrinsic absorption of about  $10^{21} \text{ cm}^{-2}$ . However, a simple single phase model with absorption in excess of the Galactic value by a factor of 2, within the inner 50 kpc, is consistent with the observed spectra.

The gravitational potential follows a NFW profile between 60 and 300 kpc, becoming flatter within 60 kpc with a power law index of about  $-0.6$  once a power law description is adopted for the total matter density. The shape of the potential is in agreement with the motion of the central dominant galaxy and suggests that the central cluster region is not relaxed.

This dark matter distribution, combined with the integrated gas mass within 300 kpc, provides a gas mass fraction ranging between 10 and 20 per cent (Fig. 16), in a good agreement with the estimate of  $0.16 \pm 0.01$  at 500 kpc from *Rosat* PSPC brightness profile and *ASCA* temperature in Ettori & Fabian (1999) and completely consistent with that generally observed in galaxy clusters (Evrard 1997, Ettori & Fabian 1999, Mohr et al. 1999).

Finally, the present *Chandra* observation of the core of A1795 allows us to resolve radially the contribution from Oxygen, Neon, Sulphur, Silicon and Iron to the plasma metallicity and, consequently, to estimate between 80 and 100 per cent the amount of Iron produced in supernova Type Ia events within the central 200 kpc.

## ACKNOWLEDGEMENTS

We thank all the staff members involved in the *Chandra* project for such an excellent performance of the instruments. ACF is grateful to NASA for the opportunity to participate to the project as an InterDisciplinary Scientist. ACF and SWA thank the Royal Society for support. We thank the referee for a careful reading of the manuscript and for several suggestions that improved the presentation of this work.

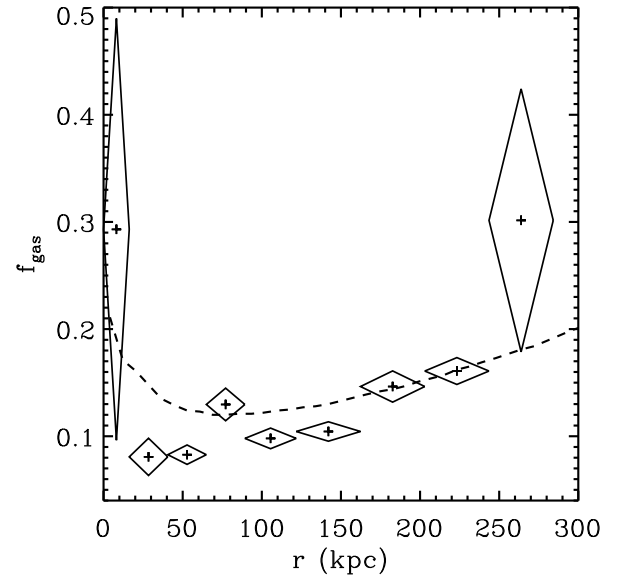


**Figure 16.** Comparison between the *spectral* (diamonds with error bars) and *spatial* (dashed line) deprojection results on the gas mass fraction.

## REFERENCES

- Abell G., Corwin H.G., Olowin R., 1989, *ApJS*, 70, 1 (ACO)
- Allen S.W., Fabian A.C., 1997, *MNRAS*, 286, 583
- Allen S.W., Fabian A.C., 1998, *MNRAS*, 297, L63
- Allen S.W., 2000, *MNRAS*, 315, 269
- Allen S.W., Fabian A.C., Johnstone R.M., Arnaud K.A., Nulsen P.E.J., 2001a, *MNRAS*, 322, 589
- Allen S.W., Ettori S., Fabian A.C., 2001b, *MNRAS*, 324, 877
- Anders E., Grevesse N., 1989, *Geochimica et Cosmochimica Acta*, 53, 197
- Arnaud M., Rothenflug R., Boulade O., Vigroux L., Vangioni-Flam E., 1992, *A&A*, 254, 49
- Arnaud K.A., 1996, "Astronomical Data Analysis Software and Systems V", eds. Jacoby G. and Barnes J., ASP Conf. Series vol. 101, 17
- Beverington P.R., Robinson D.K., 1992, *Data Reduction and Error Analysis for the Physical Sciences*, 2nd edition, McGraw-Hill Book Company
- Binney, J. & Tremaine, S., 1987, *Galactic Dynamics*, Princeton University Press, p. 226f
- Briel U.G., Henry J.P., 1996, *ApJ*, 472, 131
- Buote D., Tsai J., 1996, *ApJ*, 458, 27
- Cardiel N., Gorgas J., Aragon-Salamanca A., 1998, *MNRAS*, 298, 97
- Cavaliere A., Fusco-Femiano R., 1976, *A&A*, 49, 137
- Cowie L.L., Hu E.M., Jenkins E.B., York D.G., 1983, *ApJ*, 272, 29
- Crawford C.S., Allen S.W., Ebeling H., Edge A.C., Fabian A.C., 1999, *MNRAS*, 306, 875
- David L.P., Arnaud K., Forman W., Jones C., 1990, *ApJ*, 356, 32
- David L.P., Jones C., Forman W., Daines S.J., 1994, *ApJ*, 428, 544
- De Grandi S., Molendi S., 2001, *ApJ*, 551, 153
- De Young D., 1978, *ApJ*, 223, 47
- Dickey J.M., Lockman, F.J., 1990, *ARA&A*, 28, 215
- Dupke R.A., White III R.E., 2000, *ApJ*, 528, 139
- Dupke R.A., Arnaud K.A., 2001, *ApJ*, 548, 141
- Edge A.C., Stewart G.C., 1991, *MNRAS*, 252, 428
- Edge A.C., Stewart G.C., Fabian A.C., 1992, *MNRAS*, 258, 177
- Ettori S., Fabian A.C., 1999, *MNRAS*, 305, 834
- Ettori S., 2000, *MNRAS*, 318, 1041
- Ettori S., 2001, *MNRAS*, in press (astro-ph/0111455)
- Evrard A.E., 1997, *MNRAS* 292, 289
- Fabian A.C., 1994, *ARA&A*, 32, 227
- Fabian A.C., Johnstone R.M., Daines S.J., 1994a, *MNRAS*, 247, 439

- Fabian A.C., Arnaud K.A., Bautz M.W., Tanaka Y., 1994b, *ApJ*, 436, 63
- Fabian A.C., Mushotzky R.F., Nulsen P.E.J., Peterson J.R., 2001a, *MNRAS*, 321, L20
- Fabian A.C., Sanders J.S., Ettori S., Taylor G.B., Allen S.W., Crawford C.S., Iwasawa K., Johnstone R.M., 2001b, *MNRAS*, 321, L33
- Finoguenov A., David L.P., Ponman T.J., 2000, *ApJ*, 544, 188
- Finoguenov A., Arnaud M., David L.P., 2001, *ApJ*, 555, 191
- Fukazawa Y., Makishima K., Tamura T., Xu H., Ikebe Y., Kikuchi K., Ohashi T., 1998, *PASJ*, 50, 187
- Gibson B.K., Loewenstein M., Mushotzky R.F., 1997, *MNRAS*, 290, 623
- Grevesse N., Sauval A.J., 1998, *Space Sci. Rev.*, 85, 161
- Gunn J.E., Gott III J.R., 1972, *ApJ*, 176, 1
- Gunn K.F., Thomas P.A., 1996, *MNRAS*, 281, 1133
- Hill J.M., Hintzen P., Oegerle W.R., Romanishin W., Lesser M.P., Eisenhamer J.D., Batiski D.J., 1988, *ApJ*, 332, L23
- Hu E.M., Cowie L.L., Wang Z., 1985, *ApJS*, 59, 447
- Irwin J.A., Bregman J.N., 2001, *ApJ*, 546, 150
- Iwamoto K., Brachwitz F., Nomoto K., Kishimoto N., Umeda H., Hix W.R., Thielemann F.-K., 1999, *ApJS*, 125, 439
- Johnstone R.M., Fabian A.C., Nulsen P.E.J., 1987, *MNRAS*, 224, 75
- Johnstone R.M., Naylor T., Fabian A.C., 1991, *MNRAS*, 248, 18P
- Johnstone R.M., Fabian A.C., Edge A.C., Thomas P.A., 1992, *MNRAS*, 255, 431
- Kaastra J.S., 1992, *An X-Ray Spectral Code for Optically Thin Plasmas* (Internal SRON-Leiden Report, updated version 2.0)
- Kennicutt Jr. R.C., 1983, *ApJ*, 272, 54
- Kennicutt Jr. R.C., 1998, *ApJ*, 498, 541
- King I.R., 1962, *AJ*, 67, 471
- Kriss G.A., Cioffi D.F., Canizares C.R., 1983, *ApJ*, 272, 439
- Ishimaru Y., Arimoto N., 1997, *PASJ*, 49, 1
- Lazzati D., Chincarini G., 1998, *A&A*, 339, 52
- Liedahl D.A., Osterheld A.L., Goldstein W.H., 1995, *ApJ*, 438, L115
- Madau P., Della Valle M., Panagia N., 1998, *MNRAS*, 297, L17
- Markevitch M., Forman W.R., Sarazin C.L., Vikhlinin A., 1998, *ApJ*, 503, 77
- Markevitch M. et al., 2000, *ApJ*, 541, 542
- Markevitch M., Vikhlinin A., Mazzotta P., 2001, *ApJL*, submitted (astro-ph/0108520)
- Mazzotta P., Markevitch M., Vikhlinin A., Forman W.R., David L.P., VanSpeybroeck L., 2001, *ApJ*, 555, 205
- McLaughlin D.E., 1999, *AJ*, 117, 2398
- McNamara B.R., Januzzi B.T., Elston R., Sarazin C.L., Wise M., 1996, *ApJ*, 469, 66
- McNamara B.R., Wise M., Sarazin C.L., Januzzi B.T., Elston R., 1996, *ApJ*, L9
- Metzler C.A., Evrard A.E., 1994, *ApJ*, 437, 564
- Mittaz J.P.D. et al., 2001, *A&A*, 365, L93
- Mohr J.J., Mathiesen B., Evrard A.E., 1999, *ApJ*, 517, 627
- Molendi S., Pizzolato F., 2001, *ApJ*, 560, 194
- Moore B., Quinn T., Governato F., Stadel J., Lake Q., 1999, *MNRAS*, 310, 1147
- Mushotzky R.F., Loewenstein M., 1997, *ApJ*, 481, L63
- Navarro J.F., Frenk C.S., White S.D.M., 1997, *ApJ*, 490, 493
- Nomoto K., Hashimoto M., Tsujimoto T., Thielemann F.-K., Kishimoto N., Kubo Y., 1997a, *Nucl. Phys. A*, 616, 79
- Nomoto K., Iwamoto K., Nakasato N., Thielemann F.-K., Brachwitz F., Tsujimoto T., Kubo Y., Kishimoto N., 1997b, *Nucl. Phys. A*, 621, 467
- Oegerle W.R., Hill J.M., 1994, *AJ*, 107, 857
- Peterson J.R. et al., 2001, *A&A*, 365, L104
- Reisenegger A., Miralda-Escudé J., Waxman E., 1996, *ApJ*, 457, L11
- Renzini A., 1997, *ApJ*, 488, 35
- Sarazin C.L., 1988, *X-ray emission from clusters of galaxies*, Cambridge University Press
- Schmidt R., Allen S.W., Fabian A.C., 2001, *MNRAS*, 327, 1057
- Tamura T. et al., 2001, *A&A*, 365, L87
- Thielemann F.-K., Nomoto K., Hashimoto M.-A., 1996, *ApJ*, 460, 408
- Thomas P.A., Fabian A.C., 1990, *MNRAS*, 246, 156
- Tozzi P., Norman C., 2001, *ApJ*, 546, 63
- Vikhlinin A., Markevitch M., Murray S.S., 2001, *ApJ*, 551, 160
- Voit G.M., Donahue M., 1995, *ApJ*, 452, 164
- Weisskopf M.C., Tanabbaum H.D., Van Speybroeck L.P., O' Dell S.L., 2000, *Proc SPIE* 4012, in press (astro-ph/0004127)
- White S.D.M., Navarro J.F., Evrard A.E., Frenk C.S., 1993, *Nature*, 366, 429
- White D.A., Jones C., Forman W., 1997, *MNRAS*, 292, 419
- Wilms J., Allen A., McCray R., 2000, *ApJ*, 542, 914
- Xu H., Makishima K., Fukazawa Y., Ikebe Y., Kikuchi K., Ohashi T., Tamura T., 1998, *ApJ*, 500, 738